0.0:User notes

Although all the data supplied by the author were collected and analyzed following the scientific method, no express or implied guarantee is given. Every risk deriving from a misuse of the information provided in this thesis is taken by the user.

0.1:Abstract

Fluid-rock interactions control earthquake nucleation and the evolution of natural and man-induced seismic sequences. Experimental studies of fault frictional properties in the presence of pressurized fluids can provide unique insights into these interaction.

We performed 14 friction experiments on cohesive silicate-built (basalts) and calcite-built rocks (Carrara marbles) in the presence of pressurized pure H_2O, pure CO_2 and H_2O+CO_2 fluids to investigate the triggering of frictional instabilities associated to CO_2 storage in basalts (e.g. injection H_2O+CO_2 mixtures to fix CO_2 to newly formed carbonate minerals) and, to a less extent, the processes driving to earthquake triggering in carbonate-built rocks.

Experiments were performed at room temperature on 50/30 mm external/internal diameter hollow-shaped rock cylinders with the rotary shear apparatus SHIVA (INGV, Rome). Sample were inserted in a pressure vessel and the experiments performed under drained conditions. After imposing an initial normal stress of 15 MPa, an initial shear stress of 5 MPa and an initial pore fluid pressure of 2.5 MPa, the pore fluid pressure was increased in steps of 0.1 MPa every 100 s till the main frictional instability was triggered. The main instability was defined as the instant at which the sample accelerated to a slip rate of >0.3 m/s (seismic slip rate).

Un-deformed and deformed samples, the slip surfaces, the slipping zones and the wall rocks were investigated with optical microscope, XRD, XRF and micro-Raman spectroscopy; H_2O+CO_2 and H_2O fluids were recovered after the experiments to determine the enrichment of the chemical species (Ca^{++}, Mg^{++}, etc.).

Carrara marble was more prone to slip in the presence of pressurized H_2O+CO_2 mixtures than in pure CO_2 and H_2O fluids; instead, in basalts, the injection of pressurized H_2O+CO_2 delayed the main frictional instability with respect to the experiments performed in pure H_2O and anticipated with respect to pure CO_2 fluids. Main instabilities were preceded by creep and slip burst events ("precursory events"): the number and frequency of slip burst events was larger in the experiments performed on basalts. Moreover, in basalts enriched in clay minerals (1) fault reactivation occurred at lower pore fluid pressures at a given normal stress and (2) the frequency of precursory events decreased, making the fault more “silent” and unstable than the fault made of less altered basalts.

In the experiments, fluids may play both a chemical and mechanical role. Pure CO_2 mainly contributes to pressurize the experimental faults in both basalts and Carrara marbles, with minimal chemical interaction with the host rock.

Instead, H_2O+CO_2 mixtures resulted in formation of H^+ ions which caused dissolution of the two rock types, as suggested by the enrichment in Ca^{2+} and Mg^{2+} cations measured in their respective aqueous solutions.

Noteworthy, in the case of basalts, the high concentration of the Ca^{2+} and Mg^{2+} cations in solution and dissolved from glass, pyroxene and feldspars resulted in precipitation of calcite and dolomite (= mineral carbonation) in the experimental slipping zone. The rapid carbonation processes observed in our experiments, which last only 30-40 minutes, demonstrates the great effectiveness of the large scale CO_2 storage projects in basaltic rocks as the CarbFix in Iceland.

0.2:Riassunto

L'interazione fluido roccia controlla l'enucleazione e l'evoluzione delle sequenze sismiche naturali e indotte dall'uomo. Studi sperimentali sulle proprietà frizionali in presenza di fluidi in pressione possono fornire intuizioni uniche su queste interazioni.
Abbiamo condotto 14 esperimenti frizionali su basalti e marmi di Carrara in presenza di fluidi in pressione (H_2O pura, CO_2 pura e misture H_2O+CO_2) per investigare l'induzione di instabilità frizionali associate allo stoccaggio di CO_2 nei basalti (per esempio l'iniezione di misture H_2O+CO_2 per fissare la CO_2 ai carbonati di nuova formazione) e, in misura minore, i processi che guidano l'induzione dei terremoti in rocce carbonatiche.

Gli esperimenti sono stati condotti a temperatura ambiente su cilindri di roccia cavi con diametro esterno/interno di 50/30 mm con l'apparato di tipo rotary SHIVA installato presso l'Istituto Nazionale di Geofisica e Vulcanologia (INGV), Roma.
I campioni sono inseriti in un vessel a tenuta di pressione e gli esperimenti sono stati realizzati in condizioni drenate.
Dopo aver imposto uno sforzo normale iniziale di 15 MPa, uno sforzo di taglio iniziale di 5 MPa e una pressione di poro iniziale di 2.5 MPa, la pressione di poro è stata aumentata in gradini di 0.1 MPa ogni 100 secondi fino a che non l'instabilità frizionale non viene indotta.
L'instabilità principale è stata definita come l'istante a cui il campione accelera fino a velocità >0.3m/s (velocità sismiche).
I campioni deformati e indeformati, le superfici di slip in presenza dei fluidi, le zone di slip e gli incassanti son stati investigati con il microscopio ottico, XRD, XRF e spettroscopia micro-Raman; le acque e le misture H_2O+CO_2 sono state recuperate dopo gli esperimenti per determinare l'arricchimento nelle specie chimiche (Ca^{2+},Mg^{2+}, ecc.).
I marmi di Carrara sono più propensi a scivolare in presenza di H_2O+CO_2 in pressione rispetto all'acqua pura e alla CO_2 pura; invece, nei basalti, l'iniezione dei fluidi in pressione ha ritardato l'instabilità frizionale principale rispetto agli esperimenti eseguiti con H_2O pura e l'ha anticipata rispetto alla CO_2 pura. Le instabilità principali erano

precedute da eventi di creep e degli slip "bursts" ("eventi precursori"): il numero e la frequenza degli eventi di "slip bursts" era maggiore negli esperimenti sui basalti. Inoltre, nei basalti arricchiti nei minerali delle argille (1) la riattivazione si è verificata a più basse pressioni di poro a parità di sforzo normale e (2) la frequenza degli eventi precursori diminuisce, rendendo la faglia più "silente" e instabile rispetto alla faglia impostata su rocce meno alterate.

Negli esperimenti, i fluidi giocano sia un ruolo chimico che meccanico. La CO_2 pura contribuisce principalmente a pressurizzare la faglia sperimentale sia sui basalti che nei marmi di Carrara, con minime interazioni con la roccia incassante.

Invece, le misture H2O+CO2 sono responsabili nella formazione degli ioni H^+ che hanno causato la dissoluzione dei due tipi di roccia, come suggerito dall'arricchimento nei cationi Ca^{2+} e Mg^{2+} misurato nelle rispettive soluzioni acquose.

Degno di nota, nel caso dei basalti, l'elevata concentrazione dei cationi Ca^{2+} e Mg^{2+} in soluzione e disciolti dal vetro, pirosseni e feldspati cagionando la precipitazione di calcite e dolomite (=carbonatazione dei minerali) nella zona di slip sperimentale.

Il rapido processo di carbonatazione osservato nei nostri esperimenti, della durata di soli 30-40 minuti, dimostrano la grande efficacia dei progetti a larga scala di stoccaggio di CO_2 nelle rocce basaltiche come nel CarbFix in Islanda.

1.Introduction

Fluids play a fundamental physical (pore fluid pressure, temperature buffering, etc.) and chemical (dissolution, hydrolytic weakening, etc.) role in controlling fault strength and earthquake nucleation, propagation and arrest (e.g. Sibson, 1973,2000; Scholz, 2002). Long-lasting earthquake sequences have been associated with elevated pore fluid pressures at seismogenic depths (Miller et al.,2004).

In this regard we investigated the short term influence of H_2O and CO_2-rich pressurized fluids on the frictional strength of pre-cut experimental faults in basalts and Carrara-built marbles.

The experimental faults were loaded at the conditions that reproduce at least in part the deformation conditions expected in the upper crust, including those found at the CarbFix CO_2+H_2O injection site in Iceland (see section 1.1).These studies have implications on both in natural and human-induced seismicity.

1.1: Why investigating basalt-fluid interaction: CO_2 geological storage

Reducing anthropogenic CO_2 emissions is among the great challenges of this century.

Large scale capture and sequestration of atmospheric CO_2 has been proposed in an attempt to solve this problem and geological storage is among the suggested CO_2 sequestration methods.

The standard approach to geological storage is to inject and store CO_2 at depths >800 m in deep saline aquifers, depleted oil, gas reservoirs and barren coal seams. At these depths, CO_2 is supercritical ($T > 31.6°C$ and $P > 7.38$ MPa) and buoyant with respect to the host rocks and aqueous fluids.

The long term geological storage of buoyant supercritical CO_2 requires high-integrity cap-rock, which can be degraded through either fluid/rock interaction and/or fracturing resulting from pressure changes during and after injection (Rutqvist, 2007). In the absence of a proper impermeable cap-rock, injected CO_2 could therefore migrate laterally and upward, reducing long-term storage and contaminating the shallower groundwater resources.

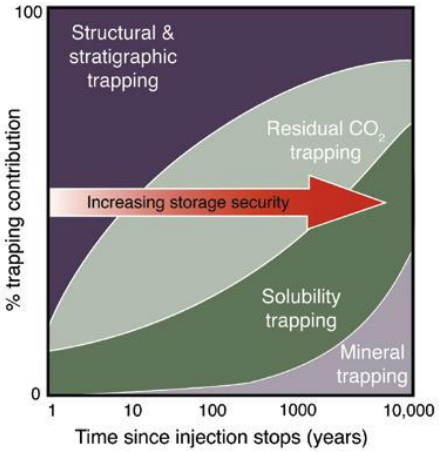

***Figure 1**: Carbon dioxide storage security*

One way to provide a long-lasting, thermodynamically stable, and environmentally benign carbon storage host is through the formation of geochemically stable carbonate minerals [12] (figure 1). After the injection into water, CO_2 will dissolve (resulting in H_2O+CO_2 mixtures), acidify water due to proton release and dissociate into bicarbonate and carbonate ions through reaction (1). Mineral carbonation requires combining CO_2-rich water with divalent metals, such as Ca^{2+},Mg^{2+} and Fe^{2+} to form carbonate minerals, such as calcite, dolomite, magnesite and siderite [5], in accord with reaction (2):

$$CO_2\ (aq) + H_2O = H_2CO_3 = HCO_3^- + H^+ = CO_3^{2-} + 2H^+ \qquad (1)$$

$$(Mg,Ca,Fe)^{2+} + CO_2 + H_2O = (Mg,Ca,Fe)CO_3 + 2H^+ \qquad (2)$$

carbonate minerals

$$(Na,Ca)Al_{1.70}Si_{2.30}O_{8\,(s)} + 6.8\ H^+ = (Na^+,Ca^{2+}) + 1.70\ Al^{3+} + 2.3\ SiO_{2\,(aq)} + 3.4\ H_2O_{\,(l)} \qquad (3)$$

Plagioclase

$$(Mg,Fe)_2SiO_{4\,(s)} + 4H^+ = (Mg,Fe)^{2+}{}_2 + SiO_{2\,(aq)} + 2\ H2O_{\,(l)} \qquad (4)$$

Olivine

$$(Ca,Mg,Fe)_2\,SiO_{3\,(s)} + 2H^+ = (Ca,Mg,Fe)^{2+}{}_2 + SiO_{2\,(aq)} + H_2O_{\,(l)} \qquad (5)$$

Pyroxene

$$SiAl_{0.36}Fe_{0.19}Mg_{0.28}Ca_{0.26}Na_{0.08}K_{0.008}O_{3.31} + 2.58\,H^+ = SiO_{2\,(aq)} + 0.36\,Al^{3+} + 0.19\,Fe^{2+}$$

Basaltic glass

$$+0.28Mg^{2+} + 0.26Ca^{2+} + 0.08K^+ +$$

$$+0.008K^+ + 1.30H_20_{(l)} \qquad (6)$$

This reaction is energetically favoured, since when CO_2 reacts with Ca, Mg, Fe oxides to form the corresponding carbonate, heat is released (exothermical reaction). Abundant metal oxides sources are silicate minerals: when silicate minerals and silicate glass come in contact with the injected acidic fluid, dissolution reaction occurs leaching divalent cations.

Given the molar concentration of oxides and the dissolution rates of various silicate minerals, the most efficient sources of the divalent cations essential for *in-situ* mineral carbonation are minerals typical of mafic and ultramafic rocks such as olivine, pyroxene, serpentine, plagioclase and basaltic glass since they are strongly under-saturated with respect to the charged injection water.

For instance, reactions (3) to (6) show the dissolution of plagioclase, pyroxene, olivine and basaltic glass and the metal oxides products, leaching out of the matrix minerals. Mineral carbonation in basalts and peridotites is a very efficient process, as observed in nature by hydrothermal alteration and surface weathering occurring in oceanic crust environments and in the laboratory inasmuch that it has been estimated that anthropogenic CO_2 injection in basalts and peridotites can provide permanent CO_2 storage on the scale of billions of tons of CO_2 per year.

Several works were conducted through basalts/peridotites-CO_2 charged water interaction from a chemical and thermodynamical point of view to evaluate the different dissolution and carbonation rates in the presence of different minerals with different pressure, temperature and pH conditions. However the frictional behavior in the presence of pressurized fluids of these rocks to be used for CO_2 storage is poorly known.

In this thesis we decided to investigate the interaction of basalts with pressurized fluids instead of peridotites for two main reasons:

1) Two large scale pilot projects are nowadays going on basaltic rocks (and none in peridotites):

-Basalt Pilot Project developed by Big Sky Carbon Sequestration Partnership (BSCSP) near Wallula (Washington, USA), in which supercritical CO_2 is injected into deep (~800 m depth) tholeiitic basalt formations belonging to Columbia River Basalt Group (CRGB);

- CarbFix pilot project at Hellisheidi (Iceland), where CO_2 charged water (H_2O+CO_2 mixtures) is injected into olivine-tholeiitic basalt sequences at a depth ranging from 400 m to 800 m. The fluid is injected at a pressure of about $P_{CO2} \simeq 2.5$ MPa, T≃25°C and pH=3.2.

In the first scenario (Columbia River Basalt Group), mineral carbonation is expected to be slower as the CO_2 has to dissolve into the groundwater to be chemically active. Hence, to limit the risks associated with buoyancy and to facilitate host rock/CO_2 interaction, it is advantageous to dissolve this gas into an aqueous solution prior to its injection into the subsurface (fully dissolved CO_2 is no longer buoyant). Thus, in the CarbFix project CO_2 and H_2O are simultaneously injected to improve security and speed up in-situ CO_2 mineralization. However, CO_2 dissolution requires large water volumes: dissolution of 1 ton of CO_2 at 2.5 MPa P_{CO2} and 25°C, requires approximately 27 tons of water (Oelkers et al, 2008). The other issue is the formation of a precipitation front that would likely plug the formation and halt CO_2-rich water injection.

2) Very low permeability in peridotites: their permeability ranges from 10^{-14} m^2 for the fractured peridotite at few hundred of meters depth to 10^{-20} m^2 at greater depths. Hence CO_2 in peridotites should be injected at high pressures and high temperatures (at least P = 8-10 MPa and T ≃ 180°C to induce engineered fracturing, to foster olivine

carbonation and thus reaction driven cracking processes. Moreover, since peridotitic rocks formed at greater depths than basalts, we speculate that they cannot work even as cap-rocks for CO_2 storage, whereas basalts may act both as reservoir and as cap-rock accordingly to their permeability and porosity.

1.2: Why investigating Carrara marbles-fluid interaction: Apennine seismic sequences

In the Apennines the upper crust is dominated by carbonate-bearing rocks (limestones and dolostones) and hosts long-lasting seismic sequences (e.g. Umbria-Marche 1997-1998, l'Aquila 2008-2009: Chiaraluce et al.,2011, Terakawa et al., 2010) associated with elevated fluid pressure at seismogenic depths (Miller at al.,2004). In fact mantle-derived CO_2 flux is widespread in central Italy and extremely vigorous ($1\text{-}3\cdot10^{11}$ mol $year^{-1}$: Chiodini et al, 2000), representing a continuous supply of fluids at the base of the brittle crust. CO_2-rich fluids in their ascent may be entrapped with encountering stratigraphic (e.g. Evaporatites or Phyllitic basement) or structural seals as documented in the Alto-Tiberina Fault (ATF). Furthermore, pressurized CO_2 may even react with water present at the base of the seal, deriving e.g. from dehydration reactions caused by fault gouge formation.

2.Methods

2.1: Experimental methods

We conducted fourteen experiments on hollow cylinders with 30/50 mm internal/external diameter of silicate-bearing (basalts) and carbonate-bearing (Carrara marbles) rocks with SHIVA , a Slow to High Rotary Apparatus, installed at the Istituto Nazionale di Geofisica e Vulcanologia (INGV) in Rome.
These experiments were performed at room temperature (~20-25°C) in the presence of pressurized fluids, that is distilled water, pure CO_2 and a combination of the two.

2.1.1: Slow to High Velocity Apparatus (SHIVA)

SHIVA imposes on the specimen quite realistic seismic deformation condition in terms of stress, velocity and acceleration. SHIVA is about 4 m long, 0.9 m wide and 1.7 m high and weights 4000 Kg. It has a horizontal setup with the rotary column on one end, the sample chamber in the middle and the stationary loading system side on the other end (figure 2a) [Di Toro et al., 2010]. Rotary motion is supplied to the samples by two brushless engines: one small engine (Ultrac III-U31320C.30.3MYZ000) and one large engine (Ultrac III-U720.30.3M00000). The small engine has an operating velocity range of 1-4000 rpm and a nominal power output of 5.15 kW. The larger motor has a maximum power output of 280 kW and a peak speed of 4000 rpm. The motors can be controlled either in torque or in velocity (displacement) mode through an inverter/controller. The engines are servoregulated through a feedback loop between the inverter/controller and an internally installed encoder and torque gage. The angular motion was measured along the rotary column with two encoders (high and low resolution) installed ~30 cm from the sample sliding surface. The high resolution optical encoder has a resolution of 0.2 μm and 629760 counts per rotation to measure

extremely low rotary speeds and the lower- resolution optical encoder has a resolution of ~400 µm and 400 counts per rotation, to measure rotary speeds above ~60 rpm (figure 2b).

Normal force is applied to the sample via an 20 kN air-actuated intensifier, acting through a lever to amplify the normal force, allowing to reach a maximum applied force of 50 kN. Normal load is measured with a 50 kN load cell (50 N resolution) installed on the "stationary" side (= non rotating shaft). Axial displacement of the nonrotating shaft is measured with a 50 mm full-scale direct current linear variable differential transformer (DCDT, ~50 µm resolution) located behind the rigid arm that halts rotational motion and with a 3 mm full-scale linear variable differential transformer (LVDT, ~0.03 µm resolution) mounted inside the sample chamber close to the sample sliding surface (figure 2c).

The nonrotating shaft is prevented from rotating by a 50 cm long arm attached to the concrete base through a vertical steel bar. Torque was measured via a S-beam type load cell (operating in extension, 3 kN full scale and 3 N resolution) located between the vertical bar and the horizontal arm (figure 2d).

a)

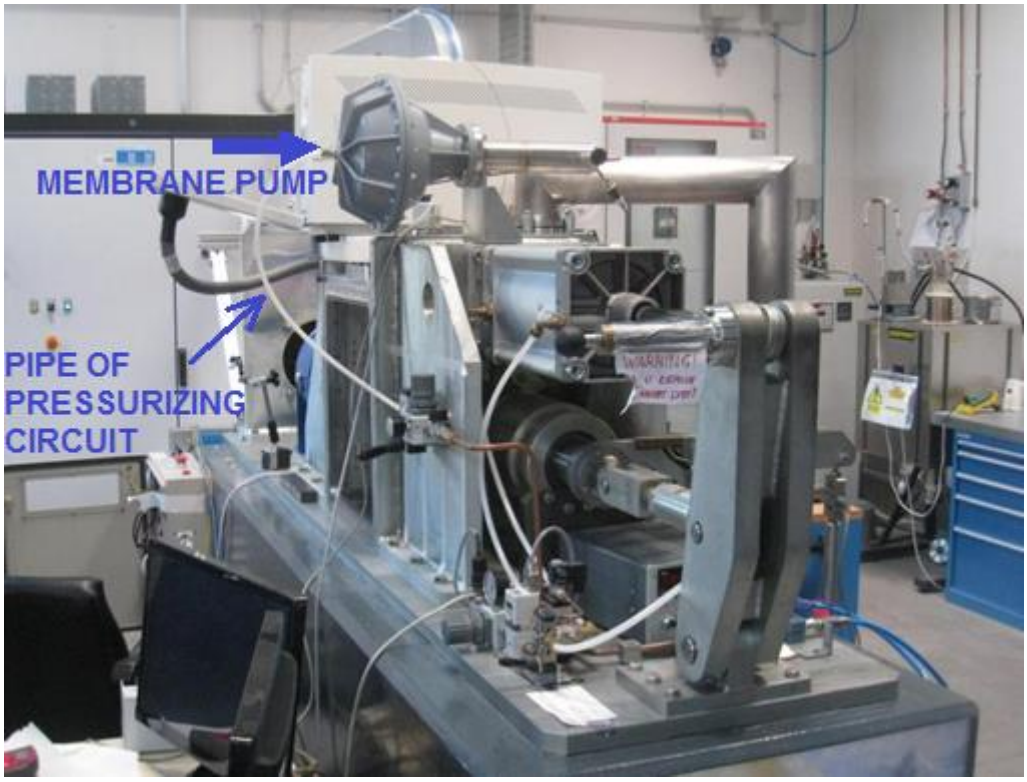

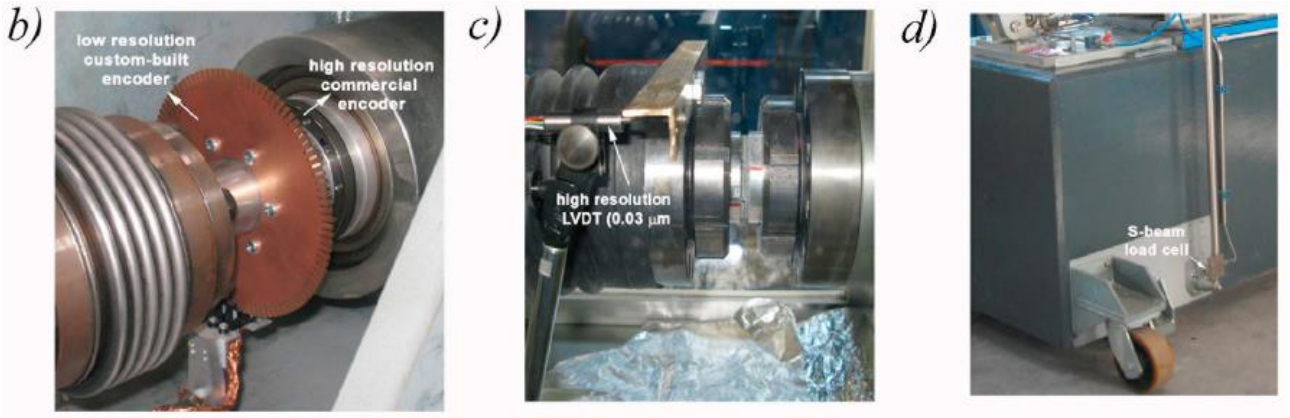

Figure 2**.: SHIVA.* ***a) *The apparatus installed at the HP/HT laboratory in Rome. In the background, the Gefran inverter/controller; in the foreground, the pressurising circuit with the membran pump and pipe (blue arrows) .* ***b)*** *The two optical encoders used to measure rotational displacement.* ***c*** *Photograph of high- resolution LVDT showing its position relative to the sample sliding surface.* ***d*** *Location of the S-beam load cell used in extension to measure the torque*

2.1.2: Experiments with H_20- and CO_2-rich fluids

2.1.2.1: Pressurizing system and pressure vessel

To perform experiments in the presence of fluids, SHIVA was equipped with a pressurizing system which consisted of a pore fluid pressure vessel (fig.3b,c), a membrane pump with a 30 cm^2 fluid capacity, a pressure multiplier that imposes up to 15 MPa of fluid pressure, a pressure regulator and valves and pipes with a 1/8 inches outside diameter (Violay et al. 2013).

During the experiments, the temperature and pressure of the fluids were monitored with sheeted K-type termocouples (precision ~ 41 μV/°C, range −200 °C to +1350 °C) and with a digital pressure sensor (precision of ± 0.1MPa) located inside the pressure vessel, close to the slip surface (~1 mm) (Fig. 3d).

All pore fluid experiments were performed under drained conditions to assure constant fluid pressure P_f and normal effective pressure σ_n' during the tests. We

performed experiments in the presence of tap water, distilled H_2O, pure CO_2 and H_2O+CO_2 mixtures, which required three different fluid pressurizing circuits and experimental procedures (fig. 3a):

Distilled water : valves A,B,C were opened and the pressure vessel was filled with water to wet the surfaces of the samples; valve C was closed to avoid fluid leakage during the tests, whereas valve A was kept open so that fluid expansion was accommodated by the movement of the membrane pump (this allowed to keep constant the P_f); σ_n was applied to bring samples into contact and finally pressurized water was applied inside the pressure vessel. After the experiment, the inlet valve A was closed, the sample was unloaded slowly and the water in the pressure vessel collected for chemical analysis. The fluid collection device (figure 3d) is made of a valve equipped with a pressure resistant gasket, connected with a tube in which unloaded fluid flows up to the collection bottle by hydraulic gradient. Collected fluid was at equilibrium with atmosphere so it was not possible to measure the dissolved gas (e.g., CO_2) concentration before fluid re-equilibrium; only the concentration of the dissolved major elements was determined (See section 2.1.2.2). In this configuration, the maximum available volume for injection fluids is $\sim$ 125 cm^3, which includes the volume of the membrane pump (30 cm^3) plus the one of the pipes and of the pressure vessel ($\sim$5 cm^3, depending on sample permeability and the amount of epoxy filling inside the hollow-shaped sample).

Pure CO_2: σ_n was applied to bring samples into contact and valve D was opened to pump pressurized CO_2 from the CO_2 tank (fig.3c) into the pressure vessel.

Mixtures of H_2O and CO_2: valves A,B,C were opened and the pressure vessel was filled with distilled water to wet the surfaces of the samples; valve A and C were closed to avoid fluid leakage during the tests and to keep a constant mass of H_2O (H_2O in the vessel was isolated from the injection sub-circuit); σ_n was applied to bring the samples into contact; we pumped the pressurized CO_2 from the CO_2 tank into the pressure vessel (valve D opened: drained conditions of CO_2 injection circuit). After the experiment the sample was unloaded slowly and the fluid in the pressure vessel collected for chemical

analysis. In this configuration the maximum available volume for the injection of fluids was $\sim 10\ cm^3$, because of the closure of valves A and C.

In both pure CO_2 and H_2O-CO_2 mixture experiments, pore pressure in the vessel was kept constant at the desired value by the pressure reducer connected to the outlet of the CO_2 tank (Fig. 3a). The pressure inside the CO_2 tank was $\sim$ 5.7 MPa at room temperature, determined by its vapour pressure, i.e. the pressure of CO_2 at the vapour phase in equilibrium with its liquid state (fig.4)

So, as long as just a tiny amount of CO_2 liquid phase is present in the CO_2 tank the internal pressure was kept constant at the vapour pressure of CO_2 (at a given temperature).

For this reason, on the inside of a closed CO_2 cylinder at equilibrium liquid-vapour, temperature is all that controls the CO_2 vapour pressure and thus temperature is all that controls the pressure in the gas tank. As a consequence, the maximum CO_2 pressure can be subjected to slight variations during the tests.

a

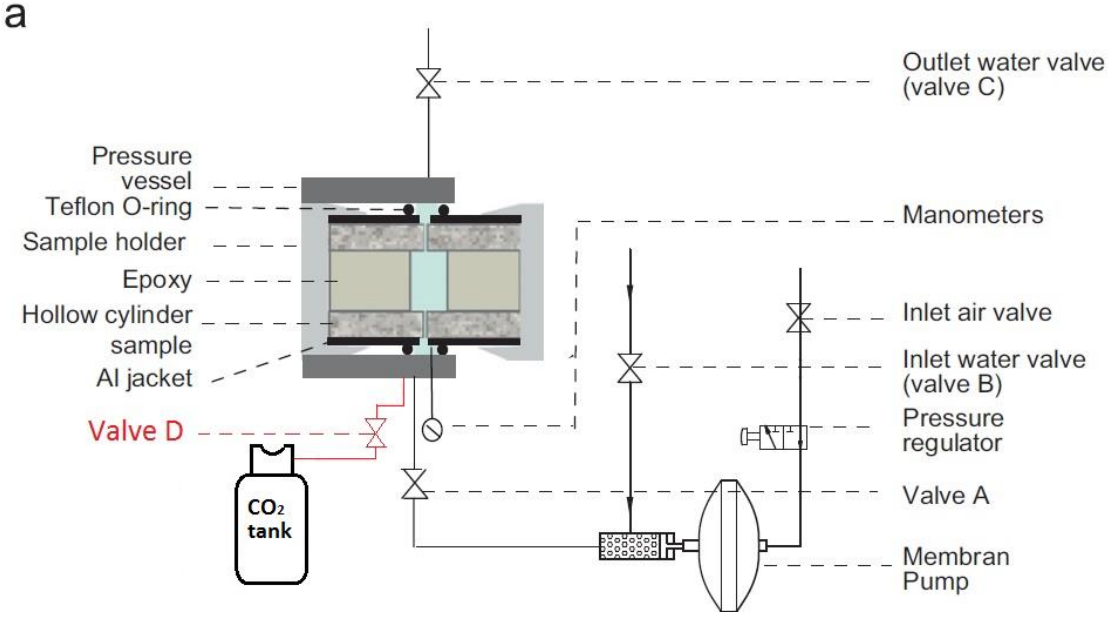
Outlet water valve
(valve C)
Pressure
vessel
Teflon O-ring
Sample holder
Epoxy
Hollow cylinder
sample
Al jacket
Valve D
CO2
tank
Manometers
Inlet air valve
Inlet water valve
(valve B)
Pressure
regulator
Valve A
Membran
Pump

b

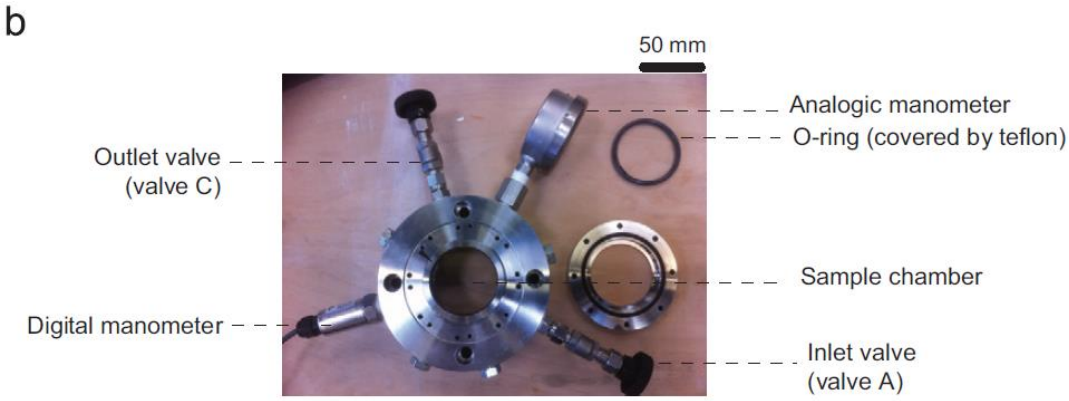
50 mm
Analogic manometer
O-ring (covered by teflon)
Outlet valve
(valve C)
Sample chamber
Digital manometer
Inlet valve
(valve A)

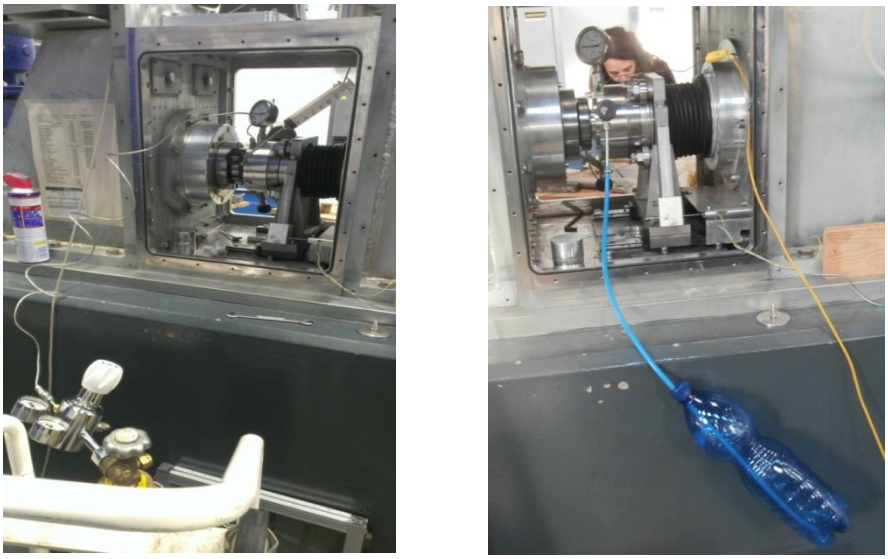

Figure 3. Experimental configuration modified after Violay et al. 2013 ***a*** *Experimental pressurization circuit. It consists of: 1) a pressure vessel, 2) a membrane pump, 3) pressure multiplier, 4) pressure regulator 5)valves and pipes.* ***b*** *Photo of the fluid pressure vessel* ***c*** *In the foreground of this photo: CO_2 tank connected to the pressurizing circuit.* ***d*** *Photo of the sample chamber: foreground of fluid collection device with light blue pipe and K-type thermocouple (yellow cable)*

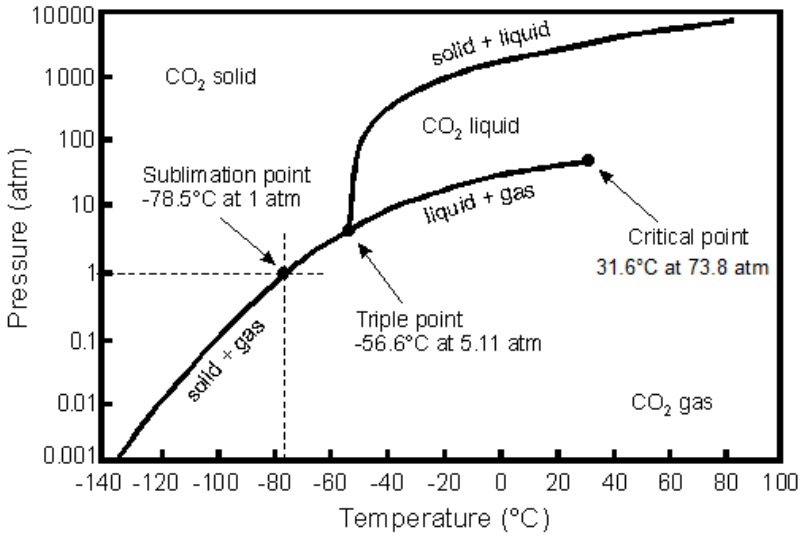

Figure 4 *:* Pressure-Temperature phase diagram for CO_2; 1atm=0.1 MPa

2.1.2.2: Evaluation of the CO_2 content in the pressurized vessel

Accurate description of the solubility of CO_2 in water is required in various scientific and technological fields, including the assessment of projects for CO_2 carbon storage.
In this regard, we estimated CO_2 solubility in distilled water at the range of temperature and pressure relevant for our studies, that is from 0.1 MPa to 6 MPa and from 15 to 25°C.
However in this work we showed a wider P-T field (i.e. 0.1 to 15 MPa and 15 to 30°C) than the investigated range achieved during experiments to better understand the sharply different behaviour of CO_2 solubility at higher pressures and lower temperatures.

Solubility of CO_2 in distilled water from 15 to 30°C and from 0.1 to 15 MPa

Figure 5a,b depict the aqueous CO_2 solubility curves (mole fraction of CO_2% and grams of CO_2 dissolved in distilled water respectively) from 15 to 30°C and from 0.1 to 15 MPa, through Diamond solubility model [Diamond et al.,2003]. The curves show that the solubility of CO_2 in water increase with increasing pressure and with decreasing temperature, as expected by the general rule of solubility of gaseous species in fluids.
However, the solubility of CO_2 in distilled H_2O is very low in the considered P-T range: the dissolved CO_2 molar fraction ranges from 0% to 3 mol% $CO_{2\ (aq)}$, (0 to ~ 70 g $CO2_{(aq)}$ /1 Kg H_2O of water).

Solubility isotherms sharply increase with pressure up to the saturation pressure (6.1 ± 0.8 MPa, depending on the temperature) then showing a clear reduction in the rate of increase (figure 5a,b: black dot).
This abrupt change in solubility trend is caused by the transition from vapour CO_2 below saturation pressure to the liquid CO_2 above this pressure. This explains why dissolved CO_2 at CarbFix working conditions (i.e. 25°C and 2.5 MPa, red dot of figure 5) is even half (33 g of $_{CO2}$ in 1 kg H2O) of the dissolved CO_2 at 15 MPa. Furthermore, it can be noticed that solubility isotherms tend to become gradually smoother approaching the lower critical end point (LCEP) of the H_2O-CO_2 binary system, located at 7.39 MPa and 31.05°C.

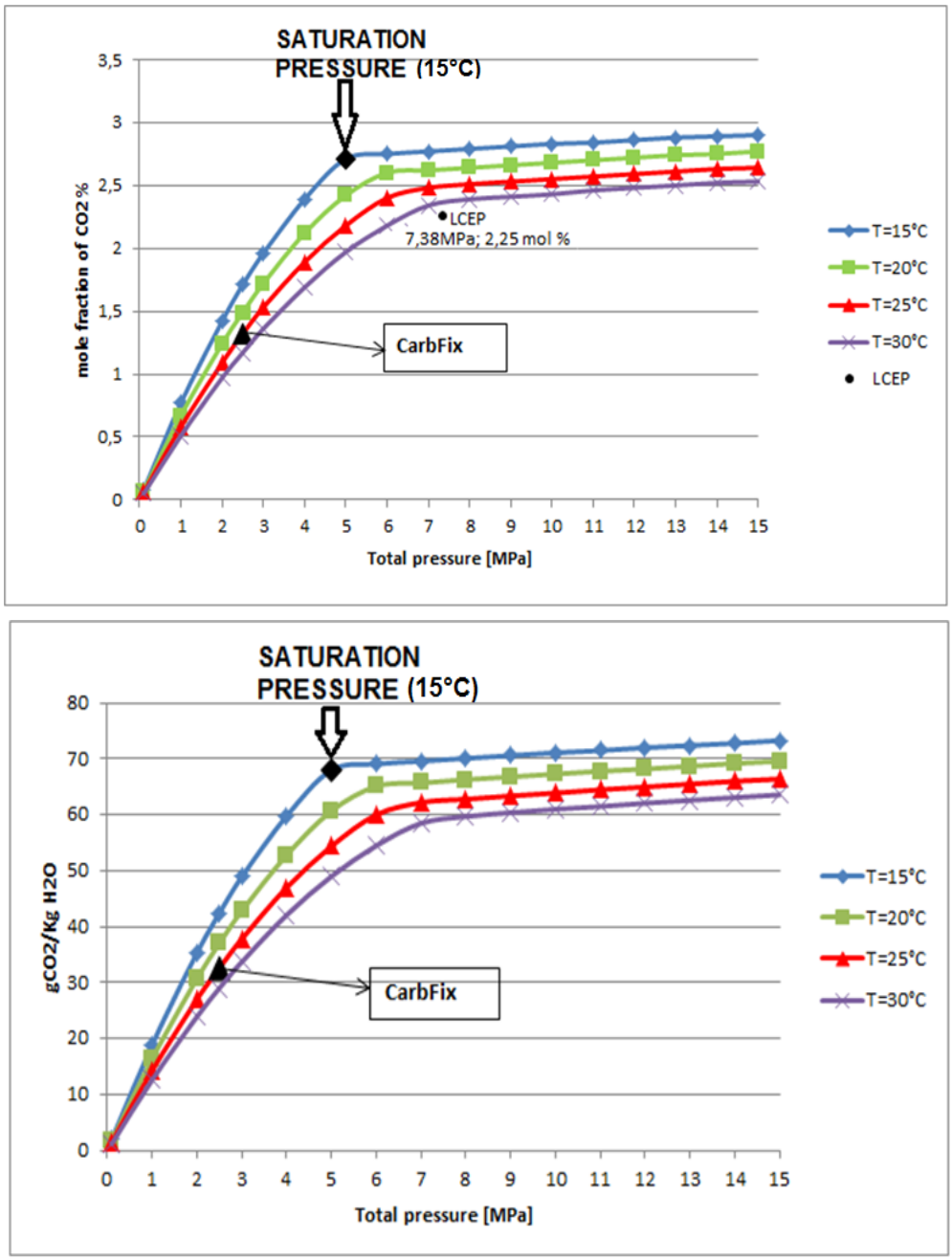

Figure 5: CO_2 evolution with pressure from 0.1 to 15 MPa and from 15 to 30°C. **a**: mole fraction as a function with total pressure.The black diamond represents the saturation pressure at 15°C, located exactly where the break in slope occurs. The black triangle marks CarbFix working conditions. The black dot is the lower critical end point, i.e. that value at which CO_2+H_2O is at the supercritical phase (lower critical end point LCEP). **b.:** grams of dissolved CO_2 per 1 Kg of H_2O solvent as a function with total pressure. The black diamond represents the saturation pressure at 15°C and the black triangle marks CarbFix working conditions.

Dissolved inorganic carbon concentration

The concentration of carbonic species ($CO_{2(aq)}$, H_2CO_3, HCO_3^- and CO_3^{2-}) and pH in the water phase were calculated starting from both the solubility of CO_2 (expressed by molar fraction of CO_2 in the aqueous phase $\chi_{CO2(aq)}$), through Diamond solubility model and the equilibrium constant for each dissociation reactions of carbonic species at the pressure and temperature range relevant in this study. For further details, we refer to Appendix A.

The effects of pressure and temperature on the concentration of carbonic species (H_2CO_3, HCO_3^{2-}) and the negative logarithm of the hydronium ion concentration H_3O^+ (pH) are shown in figures 6(a,b,c). The concentration of H_2CO_3 and HCO_3^- showed the same trends as the solubility of CO_2 in water shown in figures 4, i.e. the concentrations increased with increasing pressure whereas decreased with increasing pressure and temperature.

The pH values changed in the range of 3.9-3, decreasing with an increase in pore pressure and slightly increasing with temperature (figure 6).

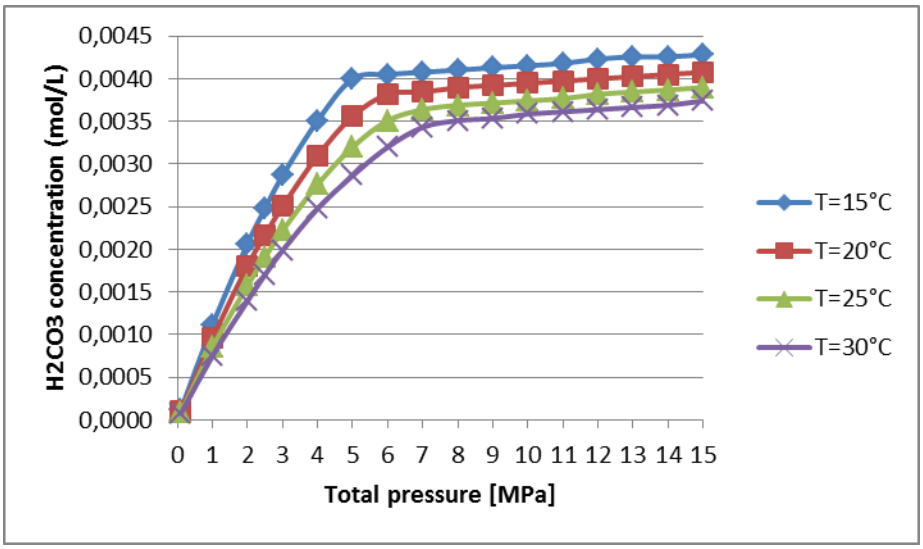

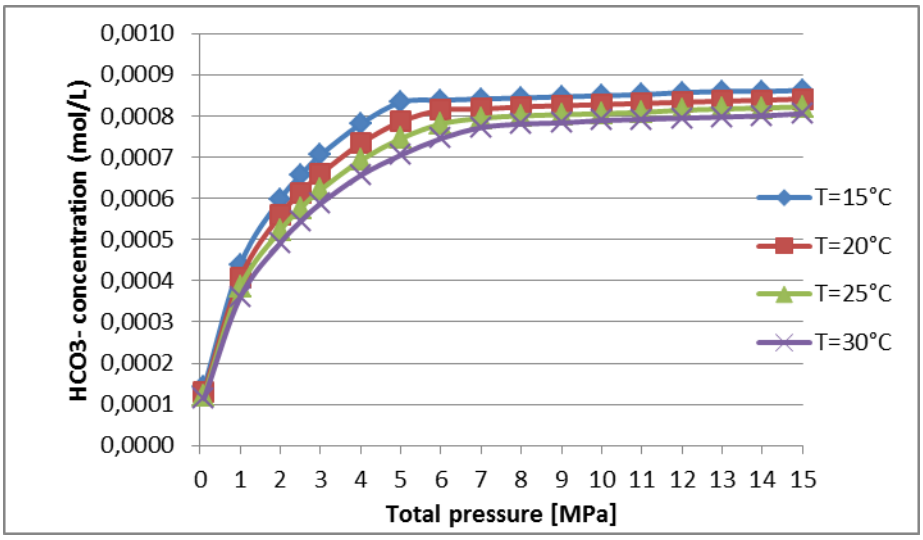

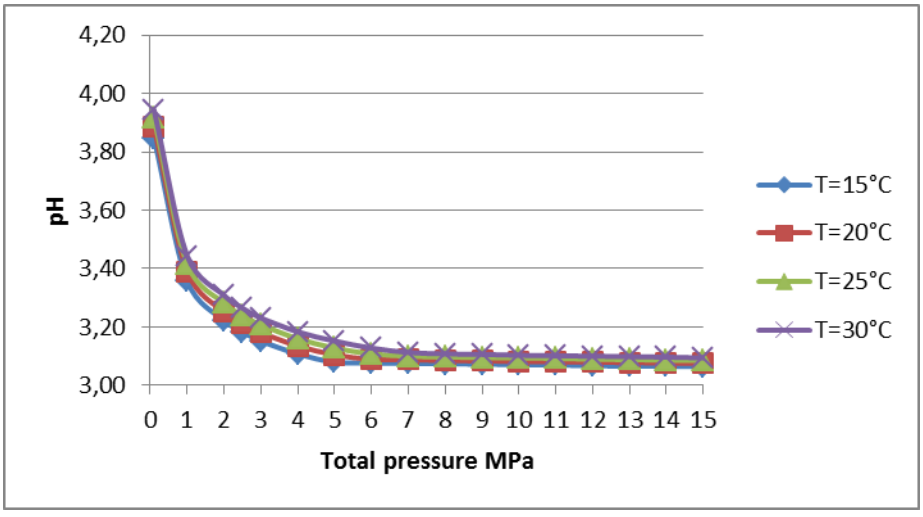

Figure 6: Top and middle page: dissolved inorganic carbon concentrations. **a** H_2CO_3 and **b** HCO_3 molarity with pressure. **c.** Bottom page: pH evolution of H_2O+CO_2 mixture with total pressure

2.1.2.3: Determination of the temperature of the rock

The temperature of the rock during the experiments was determined by thermocouples (figure 7) : temperature transducers formed by two dissimilar conductors jointed together in one point conventionally called measured junction (often referred to as the "hot" junction) ,i.e. that point exposed to heat source. The other end, formed by an appropriate two conductors extension lead, is conventionally called reference junction (also called "cold" junction) (figure 8).

Figure7: Thermocouple ending with its classical connector

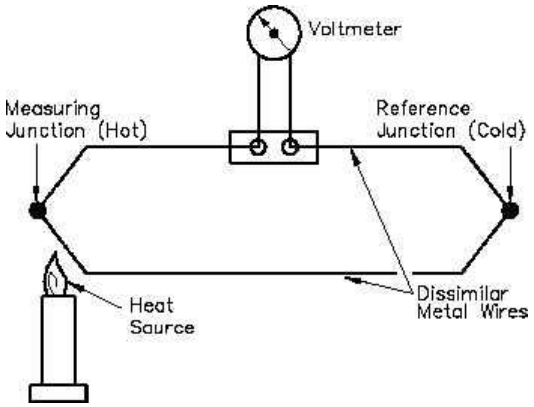

Figure8: Simple thermocouple circuit

When a temperature gradient exists between the hot and the cold junction, thermoelectric voltage is generated in the thermocouple wires, according to Seebeck effect. In our experiments we used K-type Chromel (Ni-Cr(+)) –Alumel ((Ni-Al) (-)) thermocouple, whose precision is of ~ 41 µV/°C within temperature range from −200 °C to +1350 °C. Temperature is measured through a thermoresistor. The relationship between the temperature and the electrical resistance is usually non-linear and described by a higher order polynomial:

$$R(t) = R_0 (1 + A \cdot t + B \cdot t2 + C \cdot t3 + ...) \qquad \text{Eq.1}$$

where R_0 is the nominal resistance at a specified temperature.

The number of higher order terms considered is a function of the required accuracy of measurement. The coefficients A,B and C etc. depend on the conductor material and basically define the temperature -resistance relationship. In the present work, we used a 9^{th} order polynomial function for thermocouple calibration.

During our experiments, thermocouple measuring junction was placed into an inlet valve of the pressure vessel and immersed into the fluid to measure the temperature at the boundary between the steel of the vessel and the pressurized fluid.

During all the experiment we conventionally forced first recorded temperature (before t0 defined in chapter 2.1.4.1.) equal to 23°C, because mean room temperature during our tests was about 25°C, and it is reasonable to state that steel of the pressure vessel was slightly colder than the environment.

2.1.3: Sample preparation

One key issue for a successful rotary shear experiment is the use of a very carefully and precisely shaped sample: the pair of rock cylinders must be perfectly matched, aligned and rectified to a tolerance of a few tens of microns or less, which implies a very careful preparation of the sample. In fact, imperfect parallelism between the sliding surfaces (i.e., sample misalignment) induces spurious vibrations during rotation which alter the mechanical data or induce sample failure at the initiation of sliding due to stress concentration in limited surfaces of the cylinders.

Samples mounted in the machine are prepared as a sample-mount assembly (SAMOA) following the procedure described in Nielsen et al. [2012] which ensures good parallelism of the sliding surfaces (sample misalignment < 1µm). Besides, this method is the only way found so far to allow us fluid-tight experiments with pressurized fluids (Violay et al., 2013). The procedure consists in the following steps: rock drilling, epoxy (and mortar filling) and sample grinding.

2.1.3.1: Rock drilling

Hollow cylinders of ~ 30/ 50 mm inner/outer diameter were obtained using a coaxial drill bit from saw cut ~ 40 mm thick slabs (fig. 9a,b). Hollow cylinders are preferred to solid cylinders because 1) normal load being the same, rock cylinders are subjected to greater normal stresses; 2) velocity difference is lower through the annulus with respect to solid cylinders. In fact, the tangential velocity is proportional to the radius and in the centre of the cylinder will be nominally zero. The rock hollow cylinders were clamped inside pre-cut aluminium jackets 50 mm in length with inner diameter of 50 mm and outer diameter of 54.9 mm at the bottom and 53 mm at the top. The reduced external diameter of the metal jacket allows the insertion of the sealing O-rings. The rock hollow cylinder emerges of few millimetres from the top: this will be the frictional surface during the experiments. The aluminium rings were introduced to distribute the clamping pressure on the rock cylinder (this is necessary to fix the rock cylinders to the sample holders located in the rotary and stationary columns) and, in some cases, to cover and sustain portions of the sample emerging from the holder.

Teflon (PTFE)-coated O-rings are inserted between the vessel walls and the aluminium jacket to seal the fluids inside the pressure vessel. Therefore, to avoid fluid leakage, the portion of the aluminium jacket in contact with the O-ring needs to be optically flat (mirror like surface). PTFE-covered O-rings do not react with a wide range of chemicals and have low friction coefficient, allowing smooth sliding between the aluminium external ring and the internal walls of the pressure vessel.

2.1.3.2: Epoxy and mortar filling

Once the hollow cylinders were inserted in the aluminium jackets, we sealed the bottom of the metal jacket with a latex glove. Thus we prepared a mix of epoxy resin with 25 g of resin and 3 g of hardener, poured in the inner hollow and mixed it with rock fragments from sample (figure 9c). The filling with rock fragments and core cylinder prevents excessive volume loss by shrinking of epoxy. Differently from asserted in Nielsen et al., 2012, 12 hours are sufficient for curing, even for experiments where fluid-tightness was required. Epoxy was also infiltrated between the external walls of the rock cylinder and the confining aluminium jacket.

2.1.3.3: Sample grinding

Owing to the irregular cut of the saw (e.g. the surface of the cylinder might not be orthogonal to the walls), the surfaces of the samples were rectified and grinded with a lathe (fig.9d). Once the samples were rectified, we checked the alignment of sample pairs as follows: we put the top rock portion of the pair-samples into contact.
If no light passed through, the pair samples were considered aligned and ready to be tested with SHIVA. The maximum length allowed for the rectified sample coated with the aluminium ring is 54 mm, corresponding to portion of the rock emerging of 1 to 2.5 mm.

The above technique allowed us to obtain hollow cylindrical specimens with the top and bottom surface perfectly parallel and the walls co-axial and orthogonal to the surfaces. The sample plus aluminium ring was then placed inside a stainless steel

pincer, which was subsequently placed into the sample holder. A locking ring was screwed and tightened over the pincer plus sample clamping the sample and aluminium ring assembly.

At this point the sample was ready to be mounted in the machine.

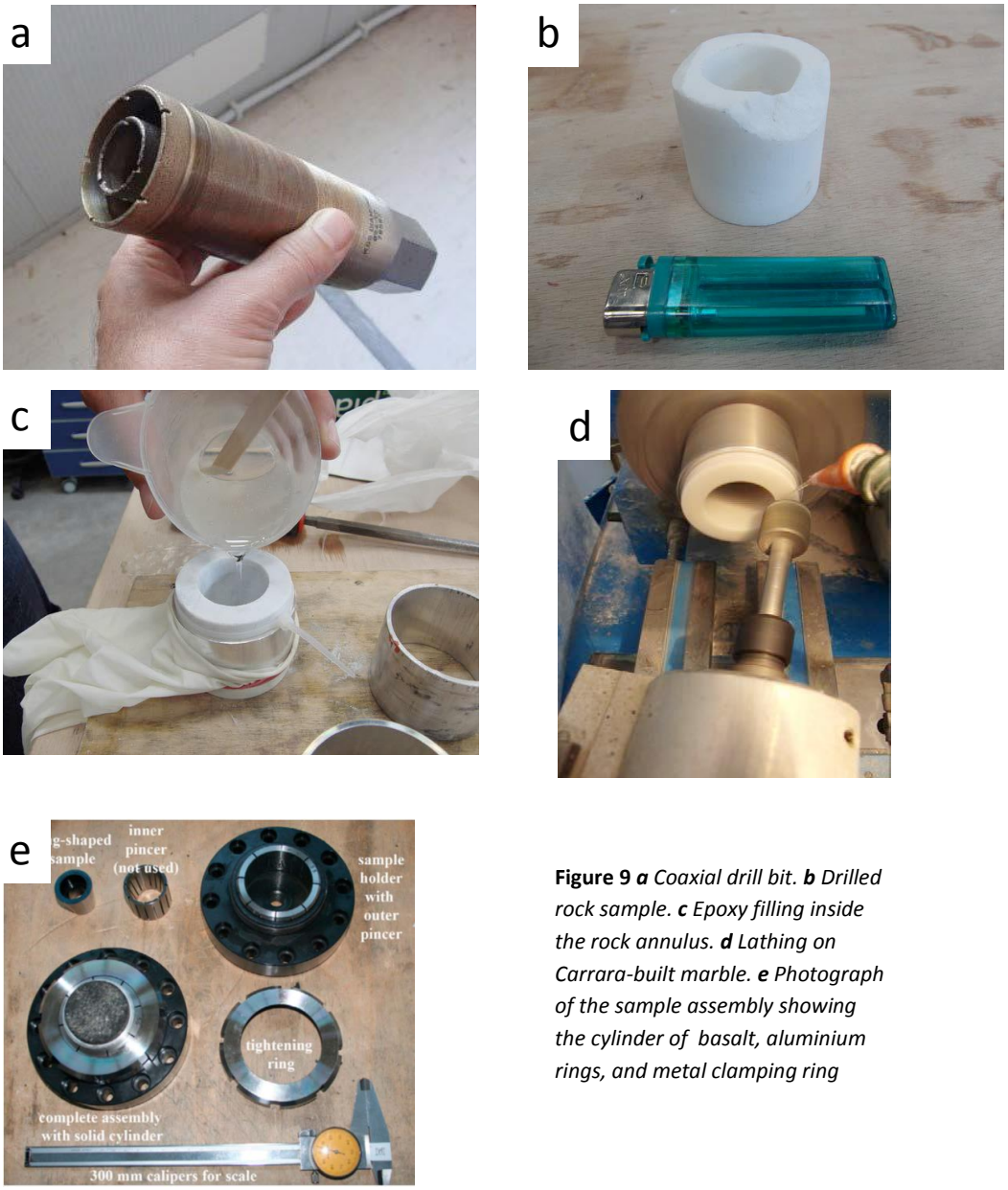

Figure 9 ***a*** *Coaxial drill bit.* ***b*** *Drilled rock sample.* ***c*** *Epoxy filling inside the rock annulus.* ***d*** *Lathing on Carrara-built marble.* ***e*** *Photograph of the sample assembly showing the cylinder of basalt, aluminium rings, and metal clamping ring*

2.1.4:Experimental procedure

2.1.4.1: Torque and pore pressure control experiments

The experiments were conducted in a configuration (given by the combination of torque and pore pressure control) called "torque and pore pressure control" (figure 10).

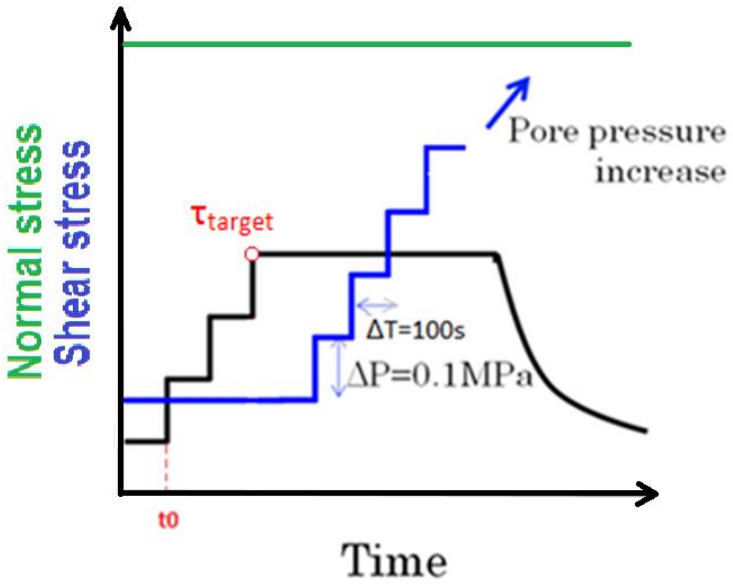

***Figure 10**: Schematic of a standard test carried out under constant shear and normal stresses and with increasing pore pressure in a configuration called "torque and pore pressure control".*

In this configuration the big engine was controlled in torque mode, which exploits the motor servoregulating system to keep the applied torque T and consequently the shear stress τ constant (Shimamoto, 1994):

$$\tau = \frac{3T}{2\pi(r_{ext}^{3} - r_{int}^{3})} \qquad Eq.2$$

where r_{ext} and r_{int} are the outer and the inner diameter of the rock ring, respectively. Pore pressure control was allowed by the drained configuration of the fluid pressurizing circuit (see section 2.1.2.1), whereas the target normal stress was kept constant thanks to the air-actuated intensifier feedback loop system.

2.1.4.2: Standard test conditions

The hollow cylinders were subjected to a normal stress σ_n = 15 MPa. After this, pore pressure was raised to 2.5 MPa and the shear stress to a target shear stress τ_{target} = 5 MPa. The τ_{target} was reached in 3 steps of 1.67 MPa every 100 s. We defined t0 as the time corresponding to the first step of shear stress increase (figure 5). The effective pressure exerted on the frictional interface results from the combined effect of the fluid pressure and the applied normal stress as expressed by 1-dimensional Terzaghi law (Paterson and Wong, 2005):

$$\sigma_{eff} = \sigma_n(1-\alpha P_f) \qquad Eq.3$$

corresponding to an effective friction coefficient of :

$$\mu_{\text{eff}} = \tau / \sigma_n (1-\alpha P_f) \qquad Eq.4$$

where α is the Biot coefficient, defined as follows:

$$\alpha = 1 - \frac{A_r}{A} \qquad Eq.5$$

in which A_r is the asperity area and A is the nominal area.

At the initiation of the experiment, from Eq. 3 μ_{eff} =0.4 (for α =1).
After this, the Pf in the vessel was increased stepwise of ΔP_f = 0.1 MPa every ~100 s to induce fault instability. We chose stepwise pore pressure increase of ~100 s to allow the Pf in the slipping zone (where the permeability could be reduced) to re-equilibrate with the Pf in the vessel: under these conditions α can be reasonably assumed equal to 1 (Paterson and Wong, 2005 and discussion therein). The experiment ends when the main instability event occurs. By main instability we refer to the condition at which the friction coefficient of the sliding rocks interface decreases resulting in an unbalance between the torque applied by the engine (τ_{target} = 5 MPa) and the strength of the experimental slipping zone ($\tau = \mu_{\text{eff}}\ \sigma_n\ (1-\alpha P_f)$ by re-arranging Eq. 2) which decreases because of the increase in P_f and, possibly, the evolution of μ_{eff} . Once the unbalanced

condition was achieved, to avoid the sample to spin to uncontrolled rotation rates, the experiments switched automatically to a velocity control mode. The velocity threshold $v_{threshold}$ was set to 0.3 m/s because the slip rate of ~ 0.1 m/s marks the transition towards large friction decrease in rocks (Di Toro et al., 2011; Goldsby and Tullis, 2011).

The only two exceptions were s1015, with $v_{threshold}$ =0.03 m/s, and s1018, with $v_{threshold}$=0.08 m/s.

2.2: Microanalytical and microphysical techniques

Pre-experimental basalt samples were analysed by optical microscope, X-Ray Fluorescence (XRF), X-Ray Powder diffraction (XRPD) and through the Helium pycnometer for geochemical, mineralogical, petrophysical and microstructural characterization.

Rock and fluid samples were recovered for post-experimental mineralogical, microstructural and geochemical analysis (with micro-Raman, SEM and ion-chromatography, respectively) to determine the deformation mechanisms and the processes responsible for any measured changes in fluid composition. Furthermore, basalt samples of the stationary side were impregnated with epoxy and cut perpendicular to the sliding surface and tangential to the slip direction for thin sectioning. Thin sections were examined under the optical microscope to verify the existence of a mineralogical and microstructural transition from the host rock to slipping zone.

2.2.1:X-ray fluorescence (XRF)

X-ray fluorescence spectrometry XRF was used to determine the bulk chemical composition of the host rocks. Elements analysed are Si, Ti, Fe, Mn, Mg, Ca, Na, K, and P (major elements, expressed in weight percent of the considered oxide); S, Sc, V, Cr, Co, Ni, Cu, Zn, Ga, Rb, Sr, Y, Zr, Nb, Ba, La, Ce, Nd, Pb, Th, U (trace elements, expressed in ppm). The instrument used is a sequential spectrometer WDS Philips PW2400 installed at the Department of Geoscience at the University of Padova. Precision is within 0.6% for major elements and 3% for trace elements. Accuracy: within 0.5% for Si, less than 3% for the other major elements, less than 5% for trace elements. Detection limits: for major elements Al, Mg and Na within 0.01%, within the 0.2% for Si, within 0.005% for Ti, Fe, Mn, Ca, K and P. Trace elements limits are expressed in ppm: Sc = 5, V = 5, Cr=6, Co = 3, Ni=3, Cu = 3, Zn=3, Ga = 5, Rb=3, Sr = 3, Y = 3, Zr=3, Nb = 3, Ba=10, La = 10, Ce=10, Nd = 10, Pb = 5, Th = 3, U = 3.

2.2.2: X-ray powder diffraction (XRPD)

Basalt specimens of few grams each were grinded with the agate and widia-built mill to produce fine powders (< 10 μm in size) for XRPD analysis to identify the mineralogical phases of rock samples. XRPD analysis were conducted at the Department of Geosciences at Padova University with a Panalytical θ-θ diffractometer (Cu radiation) equipped with a long, fine-focus Cu X-ray tube (operating at 40kV and 40mA), sample spinner, Ni filter and a solid-state detector (X'Celerator). The system optics consist of a fixed ½° divergent slit and 1° antiscatter slit on the incident beam path and soller slits (0.04 rad) on incident and diffracted beam paths. The powders were mounted on a 32-mm (internal diameter) circular sample holder. Scans were performed over the 2θ range 3-80° with a virtual step size of 0.017° in 2θ and a counting time of 100 s/step.

Phase identification and semi-quantitative analysis were performed using the software package X'Pert HighScore Plus; the phase identification was confirmed by comparison with the reference pattern database Panalytical-Inorganic Crystal Structure Database (ICSD).

2.2.3: Helium pycnometer

Effective porosity was worked out in basalt solid cylinders through the Helium-pycnometer AccuPyc II 1340 installed at the Istituto Nazionale di Geofisica e Vulcanologia (INGV, Roma). This owns three different volume chambers for the use of different sized samples and allows to measure volumes from 0.01 to 100 cm^3 with high accuracy (± 0.01% of the volume of chamber used).

2.2.4 Micro-Raman spectroscopy

Micro-Raman spectroscopy was applied for the punctual identification of the mineral phases in post-experimental cylinders. A major advantage of this micro-analytical technique is that it does not require any specific treatment of the samples, allows to

examine both thin sections and bulk samples. Micro-Raman spectroscopy was conducted at the Department of Chemistry at Padova University using the *Thermofisher* un-polarized apparatus. A green laser monochromatic light (wavelength 580 nm) was used to irradiate the sample. The laser power, directly proportional to the signal strength, varied from 2 to 5 milliwatts; the aperture controlling the amount of Raman signal reaching the spectrograph was set to a 25 μm pinhole. The estimated spot size for the instrument was 1.1 μm in diameter and the estimated spectrum resolution was 4.4 cm^{-1}.

2.2.5 Ion chromatography

Fluids samples collected after SHIVA experiments were analysed by ion-chromatography Dionex, DX500 installed at the Istituto Nazionale di Geofisica e Vulcanologia. This device measures major anions (Cl^-, SO_4^{2-}, NO_3^- and HCO_3^-) and cations (Ca^{2+}, Mg^{2+}, Na^+ and K^+). The analytical error was <5%.

2.3:Petrography and microstructure of the investigated rocks

2.3.1:CAMP and Columbia River basalts

To conduct our experiments with basalts, we selected samples from the Columbia River and CAMP Large Igneous provinces (LIPs).

Initially, we chose Columbia River basalts to simulate the CarbFix working conditions (i.e. P_f = 2.5 MPa and T = 25°C) in rocks exploited for in-situ mineral carbonation (Wallula pilot project in our study). The present work was then extended to CAMP basalts because of their analogies with Columbia River basalts concerning geochemistry, mineralogy and environmental formation: both Columbia River and CAMP basalts are continental flood basalts, i.e. they are built by voluminous sequences of lava flows which may be suitable for Carbon sequestration projects. Both CAMP and Columbia River are generally tholeiitic basalts and their main primary minerals are plagioclase, clinopyroxene (augite) and Fe-Ti oxides.

Selected basalts come from the denser part of the lava flow (lava core; figure 1) with an effective porosity ranging from 0.17 to 1 V/V% measured with He-pycnometer (see section 2.2.2) and an estimated total porosity of ~ 1.2-1.6 V/V%. We did not measure intrinsic permeability but we suppose that a reasonable range compatible with that porosity might result between 10^{-17}-10^{-20} m^2.

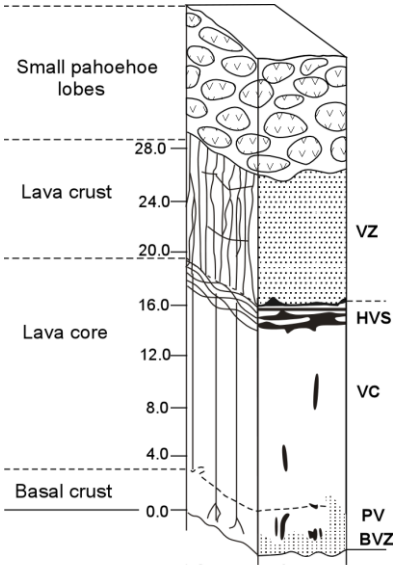

Figure11: Typical structure of continental flood basalt pahoehoe lava flows (inflated flows). The flow interior (lava core) acts as cap-rock for CO2 storage, instead the vesciculated flow top (lava crust) acts as CO2 reservoir

2.3.1.1: Petrographic observations: mineralogy, structures and textures

Thin sections of the analyzed basalts were investigated with the optical microscope.
We can subdivide basalts according to their microtexture in microporphyric, porphyric and doleritic. These features derive from the different rate of undercooling of the lava flow, thus depending on both the thickness of the flow, and the locus inside the flow of the collected sample.
Microporphyric basalts show rare phenocrysts immerged in a fine grained matrix.
The same applies to porphyric basalts, but the occurrence of phenocrysts is more frequent.
Instead, in doleritic basalts we cannot distinguish the phenocrysts from the matrix (porphyric index IP≃1). These microtexture reflects the low undercooling rate and in these cases basalts may be confused with microgabbros. During the thesis, we used for simplicity the terms fine grain size (F), medium grain size (M) and coarse grain size (C) to refer to microporphyric, porphyric and doleritic microtexture respectively. Note that in all three cases, mineral sizes never exceed 1 mm.
In the following we describe two representative porphyric Columbia River and CAMP basalts.

<u>Columbia River basalts:</u>

Phenocrysts of augite, plagioclase and opaque minerals are immersed in a matrix of randomly oriented augite and prismatic plagioclase. The rock contains also rare olivine with blackish reaction rims and partially devitrified glass (with small quantities of probable smectite).
Granophyric patches are occasionally observed. These result from late crystallization of highly viscous residual magma and are formed by alkali-feldspar and trydimite intergrowths, as confirmed by XRPD analysis .

CAMP basalts:

Phenocrysts of augite, pigeonite, plagioclase and opaque minerals are immersed in a matrix of augite, plagioclase and opaque minerals. They appear variously altered, in particular along grain boundaries (and/or fractures), yet also pervasively (distributed to almost the entire thin section).

Alteration affects olivine (altered in bowlingite/hiddingsite), pyroxene (altered in smectite/chlorite) and plagioclase (sericitization: illite + muscovite + paragonite).

Glass is usually devitrified into either smectite or chlorite depending on the temperature reached: smectites forms even at room temperature, whereas chlorite forms at temperatures of ~ 150°C (hydrothermal alteration).

2.3.1.2: Chemical and mineralogical analysis

The CAMP and Columbia River basalt samples object of our research showed differences in whole-rock chemical composition as illustrated in total alkali and silica diagram (TAS, figure 12).

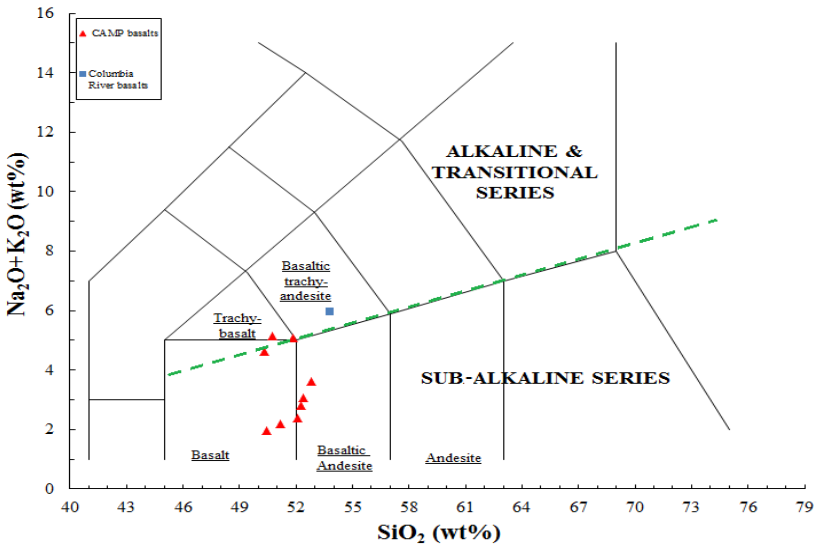

Figure 12 : TAS classification (Le Maitre,2012) of investigated basalts

CAMP basalts, which are both quartz- and olivine/hypersthene-normative belong both to sub-alkaline and transitional series, whereas quartz-normative Columbia River basalts lie just in the latter field: in fact Columbia River samples have higher alkali and silica contents with respect to CAMP basalts, as a consequence of their quite differentiated character.

Complete XRF analyses are listed in table 1.

Table 1. XRF analysis in studied basalts: note the different chemical composition and LOI values of Columbia River with respect to CAMP basalts

Sample / Ox%	CR1	CR2	AN118	NEW37	NEW70	NEW50	AN 62	AN 116	AN 127	AN 103	AN 140
SiO_2	53,79	53,76	51,83	52,24	52,10	52,41	51,14	50,73	50,34	52,81	50,46
TiO_2	2,65	2,63	1,31	1,13	1,17	0,93	1,31	1,30	1,34	1,23	0,99
Al_2O_3	13,09	13,20	14,14	14,20	14,35	13,41	13,78	13,59	13,97	14,29	14,75
Fe_2O_3	14,07	13,97	11,43	11,49	11,56	13,72	11,44	10,98	11,47	11,55	10,97
FeO											
MnO	0,18	0,18	0,16	0,17	0,21	0,22	0,20	0,14	0,15	0,18	0,18
MgO	2,43	2,58	8,09	7,65	7,63	6,74	8,13	8,32	7,84	6,55	8,11
CaO	5,93	5,87	6,88	10,87	11,13	9,60	10,80	7,41	8,25	9,30	11,80
Na_2O	3,29	3,31	4,53	2,14	1,95	2,59	1,89	3,22	2,64	1,91	1,75
K_2O	2,67	2,67	0,54	0,66	0,42	0,48	0,31	1,91	1,99	1,70	0,21
P_2O_5	0,98	0,98	0,14	0,15	0,16	0,13	0,13	0,15	0,16	0,15	0,11
Cr_2O_3							0,07	0,05	0,05	0,03	0,04
NiO							0,02	0,01	0,01	0,01	0,01
L.O.I.tot	*0,90*	*0,93*	*2,75*	0,25	1,70	0,55	0,37	2,66	2,15	0,81	1,32
tot	99,08	99,15	99,05	100,95	102,38	100,78	99,58	100,47	100,35	100,52	100,70

The more differentiated composition of Columbia River basalts is shown by their lower MgO content (~ 3 wt.%) compared to CAMP basalts (6-8 wt.%). This, combined with the quartz-normative composition of the samples, may explain the presence of reaction edges in olivine that is not in equilibrium with the Si-rich and Mg-poor host magma, so it tends to react and dissolve into it. The more differentiated composition of Columbia River basalts explains also their low CaO content (6 wt.% vs 8-11 wt.% in CAMP basalts), resulting in plg more enriched in Na than CAMP basalts. Another geochemical parameter is clearly different between Columbia River and CAMP basalts, namely loss of ignition (L.O.I.). This parameter represents the difference in weight between the untreated rock powder and the rock powder heated for about 24 hours to a temperature

of about 1000 °C. L.O.I. is thus an indicator of the presence of alteration minerals either hydrated or rich in CO_2.

As described above, most CAMP basalts are altered and in fact they show distinctly higher LOI values (up to 2.75 wt.%) than the little altered Columbia River (~0.9 wt.%)(table 1).

2.3.2:Carrara marbles

Selected Carrara marbles have on average ~300 µm grain size and >99% calcite (X-Ray Powder Diffraction Rietveld method determination, Violay et al., 2013), even though composition may slightly vary in each sample due to a) presence of thin dolomite veins and b) Mg in solid solution with Ca in calcite (the Carrara Marble tested in the experiments is amphibolitic to upper green-schist facies) (Di Toro et al., in prep.).

2.3.3: Selected hollow-cylinders couples for the experiments

Basalts:

Pair samples used during experiment were selected with different grain size to simulate reactivation of a healed fault that put in contact 2 different levels of a basaltic flow.

We tried to vary the least possible the rock properties during the tests conducted in different environmental conditions (that is same grain size, same alteration rate, etc. of the pair rock samples), but it was not always possible.

Carrara marbles:

Selected Carrara marbles were quite homogeneous in grain size, mineralogy (usually 99% of Calcite, Violay et al., 2013) and chemical composition than basalts. Therefore, the matching of the samples for the experiments did not require in depth preliminary studies like in basalts.

Selected basalts and Carrara marbles samples are listed in table 2.

Table 2: List of experiments conducted during this work: fluid involved during the test, lithology, rock name,grain size and SHIVA side of selected rock cylinders

EXPERIMENT	**Fluid**	**Basalt hollow cylinders**			
		Lithology	*Rock name*	*Grain size*	*SHIVA side*
s1015	Tap water	CAMP basalt	AN116-NEW37	Medium/Fine	Stationary/Rotary
s1019	Distilled H_2O	CAMP basalt	AN116-AN103	Medium/Medium	Stationary/Rotary
s1021	Distilled H_2O	CAMP basalt	AN140-AN62	Medium/Coarse	Stationary/Rotary
S1053	Distilled H_2O	CAMP basalt	NEW70-NEW50	Medium/Medium	Stationary/Rotary
S1055	Distilled H_2O	Columbia River basalt	CR2-CR2	Medium/Medium	Stationary/Rotary
S1016	Pure CO_2	CAMP basalt	AN116-NEW37	Medium/Fine	Stationary/Rotary
S1020	Pure CO_2	CAMP basalt	AN127-NEW50	Fine/Coarse	Stationary/Rotary
S1017	H_2O+CO_2	CAMP basalt	AN103-AN116	Medium/Medium	Stationary/Rotary
S1018	H_2O+CO_2	CAMP basalt	AN118-AN62	Fine/Coarse	Stationary/Rotary
S1054	H_2O+CO_2	Columbia River basalt	CR1-CR2	Medium/Medium	Stationary/Rotary
S1058	H_2O+CO_2	Columbia River basalt	CR2-CR1	Medium/Medium	Stationary/Rotary
S1052	Distilled H_2O	Carrara marble	M2-M1	Fine/Fine	Stationary/Rotary
S1057	Pure CO_2	Carrara marble	M5-M6	Fine/Fine	Stationary/Rotary
S1056	H_2O+CO_2	Carrara marble	M3-M4	Fine/Fine	Stationary/Rotary

3.Results

3.1: Mechanical data

In the following , we present a summary of the experimental data achieved from this study.

All experiments and their corresponding conditions are listed in Table 3.

We show the evolution of normal stress, shear stress, friction coefficient, axial shortening and slip velocity as a function of both time and slip for a typical experiment in torque and pore pressure control conducted at 15 MPa normal stress, 5 MPa shear stress, 2.5 MPa starting pore pressure with the change of the pressurized fluid involved, that is pure H_2O, pure CO_2 and H_2O+CO_2 mixture. All the mechanical data were acquired at the rate of 250 Hz.

Figure 13 shows the evolution of effective pressure, shear stress and slip velocity as a function of time in a typical experiment conducted both with basalt and Carrara marbles pair-samples.

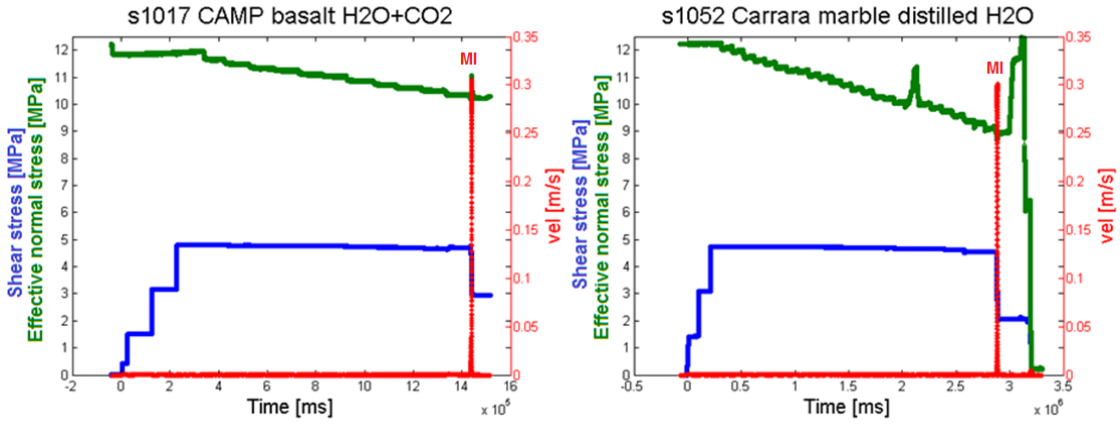

Figure13: *Typical experiments conducted in torque and pore pressure control: evolution of effective pressure, slip velocity and shear stress as a function of time in basalt and Carrara marble.*
MI marks the main instability.

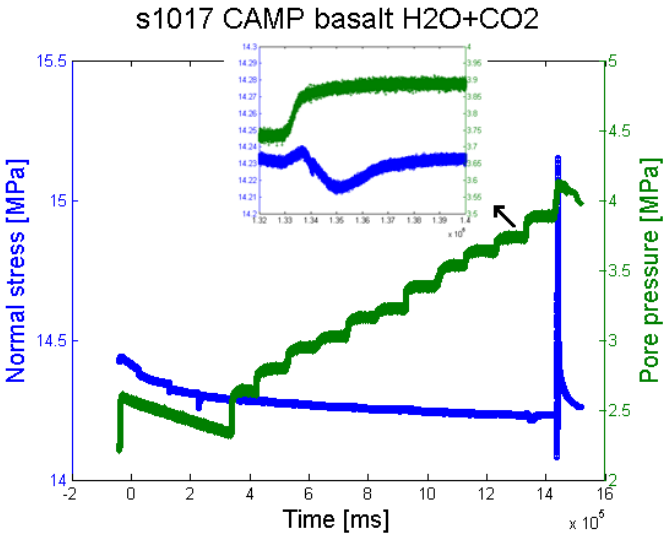

***Figure 14**: Normal stress and pore pressure versus time during a typical experiment. The inset show details during a pore pressure increasing step.*

After about 300 s, once the target shear stress (τ_t = 5 MPa) and the effective stress (12.5 MPa) were achieved, we imposed the stepwise increase in pore fluid pressure of ~ 0.1-0.2 MPa every ~100 s which resulted in a stepwise decrease of the effective pressure of the same amount (green curves). The steps in pore fluid pressure triggered shear stress variations (blue curves) and slip (creep-like) events (red curves) (Figure 13).

Precursory events (see Fig. 20), that is the events preceding the main instability (MI in Fig. 13), may cause shear stress variations $\Delta\tau$ of approximately 0.1-0.2 MPa. However, as the motor is in control mode, it restores the imposed τ_t of about 5 MPa in a time frame of ~60 μs (this is the feedback time between the torque gage of the engine and the inverter that controls the electric power absorbed by the motor to impose a shear stress of 5 MPa). However, in some experiments, we documented an oscillation of τ_t from 4.5 to 4.9 MPa. Instead, during the main instability event, shear stress drops rapidly and since the control system imposes the τ_t of 5 MPa, the sample is abruptly accelerated (i.e., there is a low frictional resistance against the imposed shear stress). To avoid the sample to achieve nominally infinite slip rates, the sample equivalent velocity was limited to 300 mm s^{-1}.

Normal stress is kept constant by the air actuator during the tests, but once the main instability is triggered, an overshooting in normal stress occurs owing to the abrupt strength loss of the experimental fault (blue curve in Fig. 14). However if we zoom the graph, we notice that the normal stress, during the pore pressure increase, first increases abruptly and then decays to reach a constant value (the normal stress evolution with time is similar to a triangular wave: figure 14, inset). This normal stress decrease indicates that the air-actuated system is not able to keep up with the imposed fast pore pressure increase and it takes few ms to stabilize. However, the drop in normal stress is of about 0.02 MPa, negligible compared to the 15 MPa of imposed normal stress.

An overall view of the frictional evolution of the experimental fault versus time and slip is shown in figure 15.

The figure includes a 3-D plot Time vs slip vs Friction comprehensive of its 2D front views Friction vs Time and Friction vs slip. The 3D plot allowed us to follow the evolution of friction with time and the displacement cumulated at that time. From these plots, we noticed that friction increases with decreasing normal stress and with increasing pore pressure and shear stress, as expected by Eq.4.

Furthermore, we noticed that the friction instability oscillation with slip during the main instability is controlled by velocity variations: the higher is the slip velocity, the lower is the friction coefficient (i.e., velocity-weakening behavior) (fig.15).

***Table 3**: List of experiments. See text for details*

Exp	Rock type	Fluid	Notes
s1015	CAMP basalt	Tap H_2O	Speed limiting device fixed to 0.03 m/s; failure to register encoder1 signal
s1016	CAMP basalt	Pure CO_2	/
s1017	CAMP basalt	H_2O+CO_2	/
s1018	CAMP basalt	H_2O+CO_2	Main instability at v=0.07 m/s even if speed limiting device was set to 0.3 m/s
s1019	CAMP basalt	Distilled H_2O	/
s1020	CAMP basalt	Pure CO_2	/
s1021	CAMP basalt	Distilled H_2O	Rotation of sample holder from 300s to 450 s corresponding to 4.7 Pp
s1052	Carrara marble	Distilled H_2O	LVDT absent
s1053	CAMP basalt	Distilled H_2O	LVDT absent; issues in pore pressure control concomitant to fluid leakage
s1054	Columbia River basalt	H_2O+CO_2	Normal stress decreasing in 3 steps of 0.5 MPa every 100s to induce fault instability (from 3050s to 3150s). Huge amount of fluid leakage. LVDT absent
s1055	Columbia River basalt	Distilled H_2O	LVDT absent
s1056	Carrara marble	H_2O+CO_2	LVDT absent
s1057	Carrara marble	Pure CO_2	Decreasing of 0.5 MPa normal stress at $\sim$ 2828 s to induce fault instability . LVDT absent

s1058	Columbia River basalt	H_2O+CO_2	Decreasing of 0.5 MPa normal stress at ~ 2827 s to induce fault instability. LVDT absent.

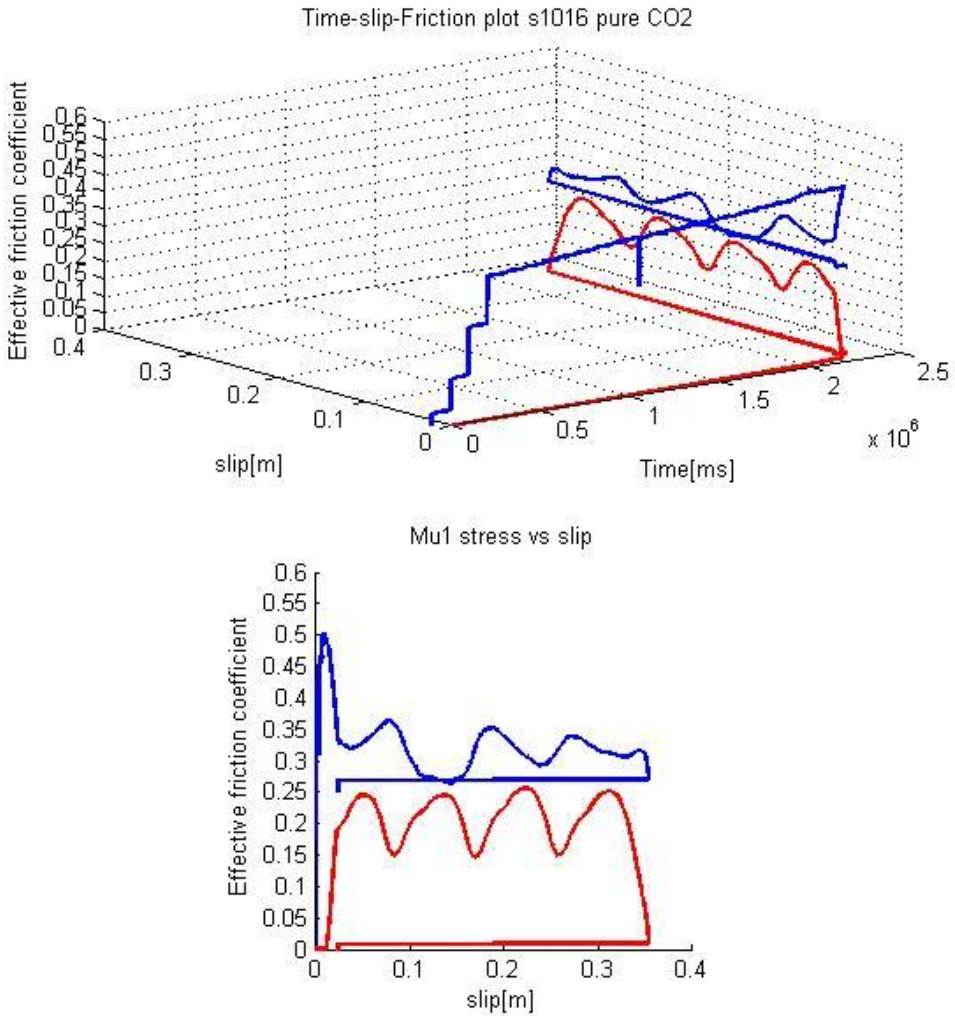

Figure 15: *3D plot time vs slip vs friction & slip velocity of a typical experiment and its 2D front view friction vs slip and friction vs time.*

To quantify the frictional behavior of the two rocks, we measured for each experiment peak parameters, the slip weakening distance, LVDT data and analyzed the precursory events.

3.1.1: Main instabilities events

Peak parameters (Figs 16,17) were obtained starting from the same type of graph described in figure 13 with the following procedure:

1) we determined the instant t_{peak} when the peak shear stress $\tau_{peak,}$ was achieved

2) we determined the $\sigma'_{peak,}$ $\mu_{eff\ peak}$ and $slip_{peak}$ at t_{peak}.

The main instability parameters for basalts and Carrara marbles are summarized in table 4-5 and Figs. 16-17.

3.1.1.1: Basalts

Main mechanical parameters prior the onset of instability are listed in Table 4

***Table 4**: Main mechanical parameters of basalts prior to the onset of instability (peak parameters at time t_{peak}). This table is divided in 3 rows to subdivide H_2O, CO_2 and H_2O+CO_2*

Experiment	*Fluid involved*	*Peak of effective normal stress: $\sigma'_{peak}= \sigma_{n\ peak} - Pp_{peak}$ [MPa]*	*Peak of normal stress: $\sigma_{n\ peak}$ [MPa]*	*Peak of effective friction coefficient: $\mu_{eff\ peak}$*	*Peak of slip: $slip_{peak}$ [m] (cumulative slip before main instability)*	*Peak of shear stress τ_{peak} [MPa]*
s1015	Tap H2O	10.3	14.7	0.47	0.031	*4.82*
s1019	Distilled H2O	10.3	14.5	0.46	0.018	4.74
s1021	Distilled H2O	9.5	14.4	0.48	0.039	*4.59*
s1053	Distilled H2O	9.9	15.1	0.45	0.035	4.43
s1055	Distilled H2O	9.5	14.5	0.47	0.060	4.42
s1016	Pure CO2	9.7	14.6	0.49	0.013	4.75
s1020	Pure CO2	9.4	14.2	0.49	0.022	4.64

s1017	H2O+CO2	10.2	14.2	0.47	0.008	4.74
s1018	H2O+CO2	10.2	14.8	0.46	0.034	4.85
s1054	H2O+CO2	8.3	13.0	0.58	0.095	4.85
s1058	H2O+CO2	8.7	14.9	0.52	0.043	4.52

In the experiments conducted with basalts, fault instability occurred at a peak of shear stress ranging from 4.42 MPa to 4.85 MPa, an effective pressure between 8.7 MPa and 10.3 MPa, (corresponding to an effective friction coefficient between 0.45 and 0.58); cumulative slip prior to the main instability ranges from 0.008 to 0.095 m (Figure 4).
In s1055, s1017, s1018, s1054 we observed that τ_{peak} is influenced by τ_t.

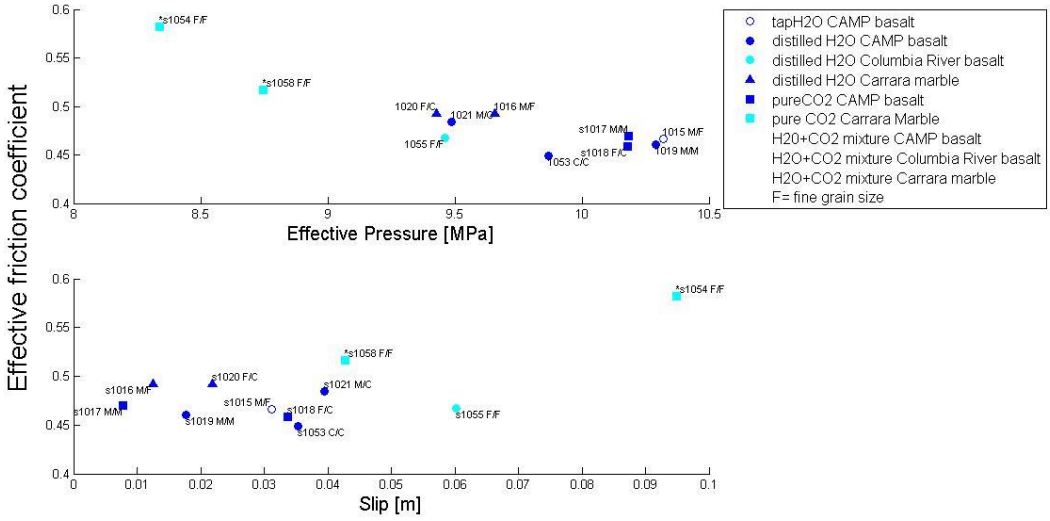

Figure 16*:* Synoptic chart indicating peak parameters collected during experiments with basalts. *In the top panel* : peak shear stress against effective pressure. In the middle: effective friction coefficient vs effective pressure. At the bottom panel: effective friction coefficient against slip

We observe that s1054 and 1058, immersed in H_2O+CO_2 have the lowest effective normal stress (and, as a consequence, highest pore pressures relative to the imposed normal stress) at the time of the main instability. As a matter of fact, and differently to all the other experiments, during these two tests we had to reduce the normal stress of 0.5 MPa to reactivate the experimental fault because we reached the maximum pressure limit of the CO_2 tank before the main instability was triggered.

3.1.1.2: Carrara marbles

***Table 5**: Main mechanical parameters in Carrara marble prior to the onset of the main instability (peak parameters). This table is divided in 3 rows to subdivide H_2O, CO_2 and H_2O+CO_2*

Experiment	*Fluid involved*	*Peak of effective normal stress:* $\sigma'_{peak}= \sigma_{n,peak}- Pf_{peak}$ *[MPa]*	*Peak of normal stress:* $\sigma_{n\ peak}$ *[MPa]*	*Peak of effective friction coefficient:* $\mu_{eff\ peak}$	*Peak of slip:* $slip_{peak}$ *[m] (cumulative slip before main instability)*	*Peak of shear stress* τ_{peak} *[MPa]*
s1052	Distilled H_2O	9.0	14.9	0.50	0.015	4.49
s1057	Pure CO_2	9.5	14.5	0.47	0.020	4.47
s1056	H_2O+CO_2	9.8	14.6	0.50	0.021	4.82

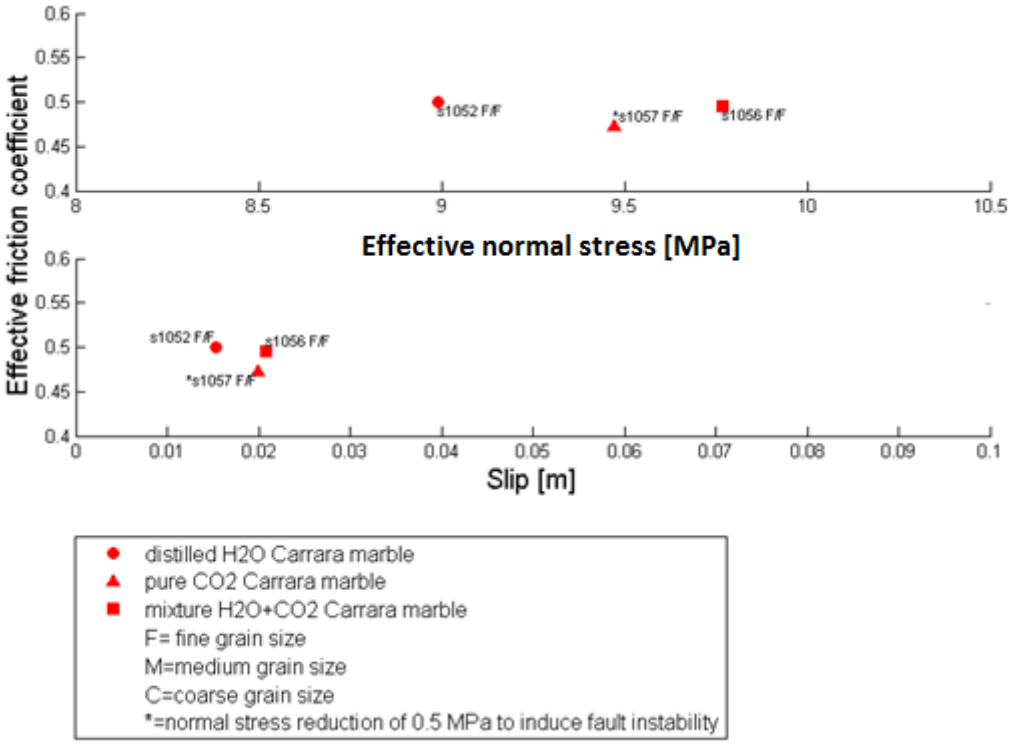

Figure 17*: synoptic chart showing peak parameters collected during experiments with Carrara marbles. In the top panel* : peak shear stress against effective pressure. In the middle: effective friction coefficient vs effective pressure. At the bottom panel: effective friction coefficient against slip

Table 5 and figure 17 show that in the experiments conducted with Carrara marbles , fault instability occurred at a peak of shear stress ranging from 4.56 MPa to 4.81 MPa, an effective pressure between 9.0 MPa and 9.8 MPa, corresponding to peak of friction coefficient between 0.45 and 0.50, whereas cumulative slip prior to the main instability ranges from 0.015 to 0.021 m.

Hence, data points are very close in particular in terms of slip cumulated prior the main instability.

Furthermore these data suggest that main fault instability occurs at a greater pore pressure (thus at lower normal effective pressure) when the sample was immersed in H_2O than in CO_2 and H_2O+CO_2.

3.1.2:Slip weakening distance Dw_1

The friction coefficient decays with time and slip. We defined the slip weakening slip distance Dw_1 as the distance corresponding to 100% of friction decay (from μ_{peak} to $\mu_{dynamic}$). We also defined the slip cumulated prior instability, $slip_{peak}$ and the $slip_{total}$ = $slip_{peak}$ + Dw1.

These values are extracted through the plot of friction coefficient against slip and listed in table 6. These data allowed to calculate friction percentage drop, defined as $(\mu_{peak}-\mu_{dynamic} / \mu_{peak})\cdot 100$.

In these plots, we preferred to use slip recorded through the high resolution encoder 1 (Slip Enc_1), instead of the slip derived from the combination of the two encoder as our interest was focused to the friction decay corresponding to the onset of instability; in fact during main instability event, friction oscillates with slip because of its dependence with velocity (figure 15 and s1015-fig.18). Moreover, friction oscillation during slip impeded us to calculate a reasonable value of steady state friction.

3.1.2.1 Dw1 in basalts

We made friction vs slip enc_1 plots for the three typical experiments (fig.18) and extracted the main results in table 6.

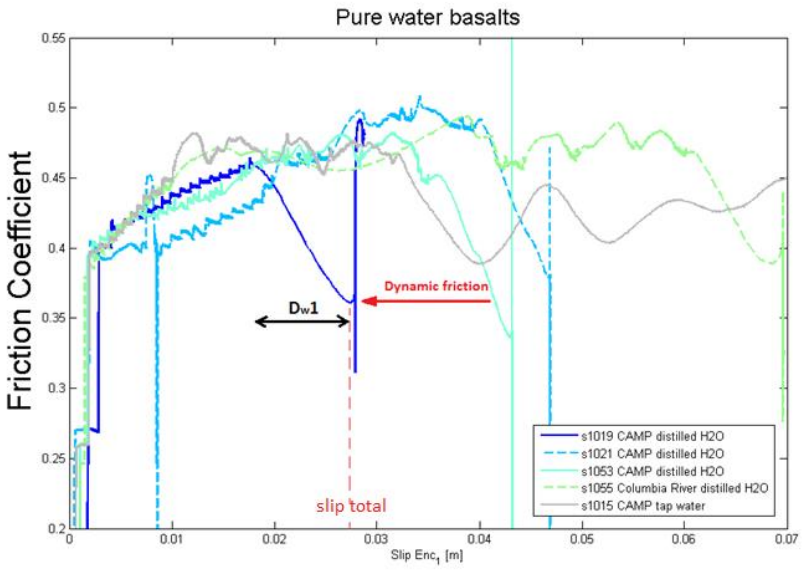

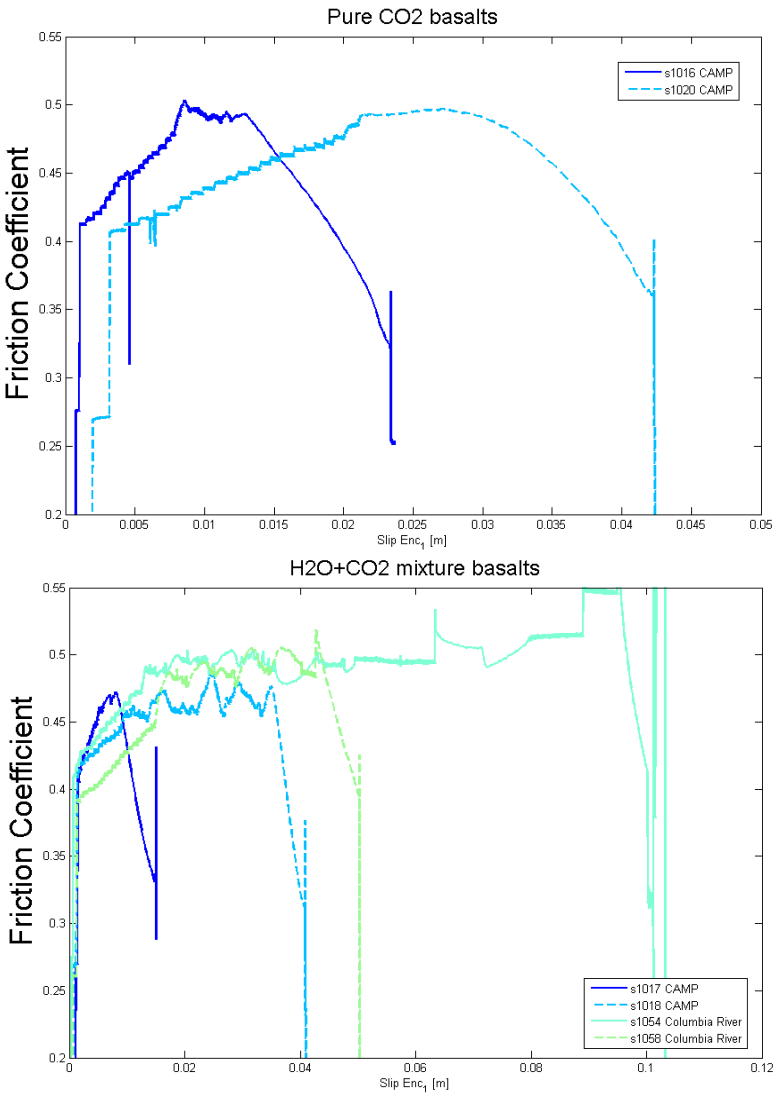

Figure 18: *friction coefficient vs slip enc1 plots in basalts a)pure water, b)pure CO_2, c)H_2O+CO_2 mixture necessary to extract Dw1 and friction loss*

***Table 6**: List of basalts data extracted from figure 18*

Exp.	Fluid involved	Peak Slip [m]	Dw1 [m]	$slip_{total}$ [m]	Peak of Friction Coefficient	Dynamic friction	Friction drop %
s1015	Tap water	0,031	0.009	0,040	0.47	0.39	17
s1019	Distilled H_2O	0.018	0.009	0.027	0.46	0.36	22
s1021	Distilled H_2O	0.039	0,008	0,047	0.48	0.38	21
s1053	Distilled H_2O	0.035	0,008	0,043	0.45	0.34	24
s1055	Distilled H_2O	0.060	0,008	0,068	0,47	0.39	17
s1016	Pure CO_2	0.013	0.01	0.023	0.49	0.32	35
s1020	Pure CO_2	0.022	0.02	0.042	0.49	0.36	27
s1017	H_2O+CO_2	0.008	0.007	0.015	0.47	0.33	30
s1018	H_2O+CO_2	0.034	0.007	0.041	0.46	0.31	33
s1054	H_2O+CO_2	0.095	0,006	0,101	0.58	0.32	45
s1058	H_2O+CO_2	0.043	0,007	0,050	0.52	0.39	25

Table 4 suggests that Dw1 in basalts during experiments is rather similar: except for s1020 whose Dw1= 0.02 m, in the other tests it ranges from 0.006 to 0.01 m, independently of the pressurized fluid used.

Contrarily, friction drop % has a wider range: in H_2O-bearing experiments is c. 20%, instead in both pure CO_2 and H_2O+CO_2 experiments Dw1 is ~30 %.

3.1.2.2 Dw1 in Carrara marbles

Pure H_2O, pure CO_2 and H_2O+CO_2 experiments were plotted together because of the limited number of experiments (figure 19). The frictional data are remarkably similar independently of the environmental conditions: the Dw1 ranges between 0.007 m and 0.012 m and the friction drop % is 32-34% (Table 5). However, s1057 sheared in pure CO_2 fluid has a smoother friction decay than in presence of H_2O and H_2O+CO_2 mixtures (Fig. 7).

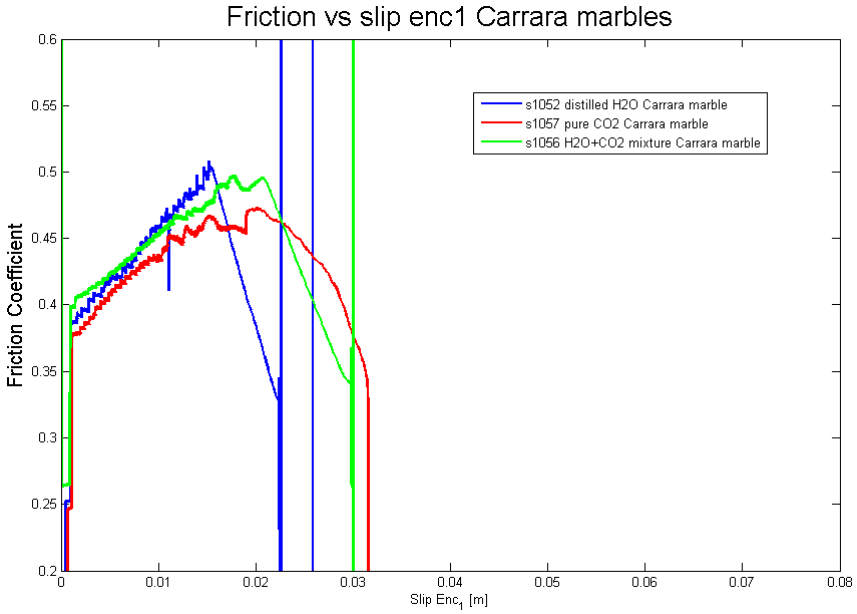

Figure 19: *friction coefficient vs slip enc1 plot necessary to extract Dw1 and friction drop*

***Table 7**: List of basalts data extracted from figure 19*

Exp.	Fluid involved	Peak of Slip [m]	Dw1 [m]	$slip_{total}$ [m]	Peak of Friction Coefficient	Dynamic friction	Friction drop %
s1052	Distilled H_2O	0.015	0,007	0,022	0.50	0.33	34
s1057	Pure CO_2	0.020	0.012	0.032	0.47	0.32	32
s1056	H_2O+CO_2	0.021	0,009	0,030	0.50	0.34	32

3.1.3 Precursory events

Precursory events are analyzed using the same plot of figure 13, but at higher magnification regarding the velocity evolution with slip to identify the slip events marked by velocity pulses significantly lower than the main instability event (figure 20).

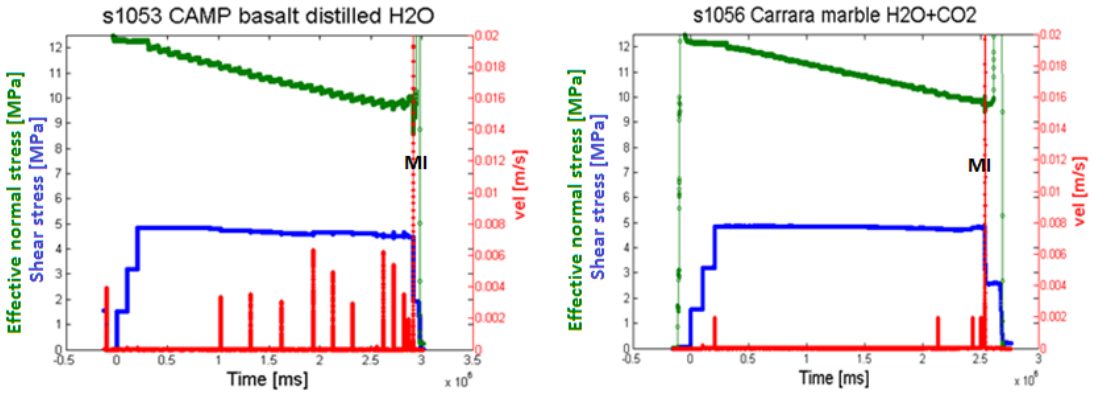

***Figure 20:** Typical experiments conducted in torque and pore pressure control: evolution of effective pressure, slip velocity and shear stress as a function of time in basalts and Carrara marbles. Differently from figure 13, we mainly focused on precursory events (red lines) to the main instability (MI in the diagram).*

We worked out for each experiment the relative cumulative frequency curve as a function of slip, firstly to choice a reasonable slip velocity lower threshold (figure 21). Relative cumulative frequency was calculated using Weibull frequency formula of frequency:

$$F(x_i)= i/(N+1) \qquad Eq.6$$

with i (1 < i < N) the number of slip velocity observations ≤ of an assigned value and N the sample size.

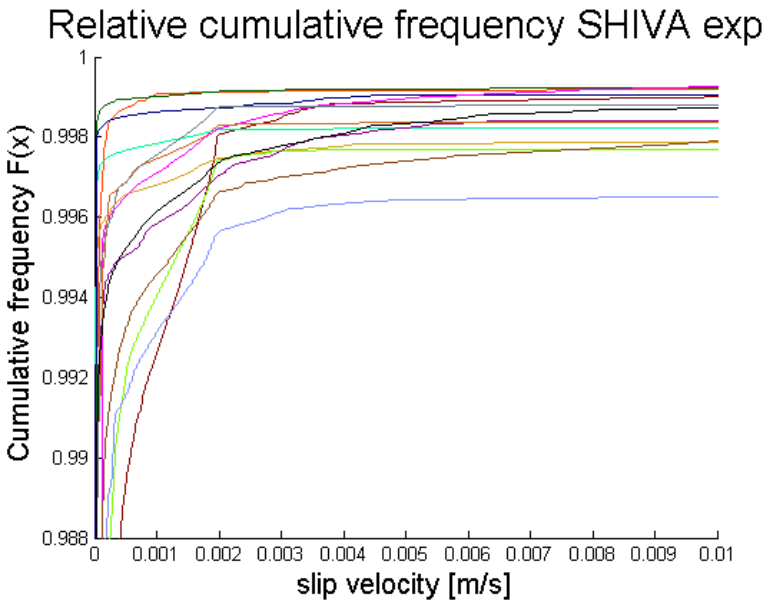

Figure 21: *Overall view of all relative cumulative frequencies as a function of slip velocity*

The summary plot in Fig. 21 (all basalt and Carrara marble dataset) shows that events with slip velocity $<10^{-3}$ m/s may occur with very high frequency: we decided to consider these events as background noise and discard them. We set the threshold value to 10^{-3} m/s, that is the value where slope changes in most curves and hence where cumulative frequency exceeding a certain slip velocity value start to decrease significantly. Precursory event counting was done for each experiment using figure 20-

like plots and listed in tables 8-9. Basalt data were subdivided into the three different environmental conditions (Fig 22 a = H_2O; Fig 22 b = CO_2; Fig.22 c = H_2O+CO_2), whereas the relative frequency distributions of Carrara marbles immersed in H_2O, CO_2 and H_2O+CO_2 were plotted all together (Fig. 23).

3.1.3.1 Precursory events: basalts

Basalts cumulated frequency curves and some of the precursory events plots are shown below.

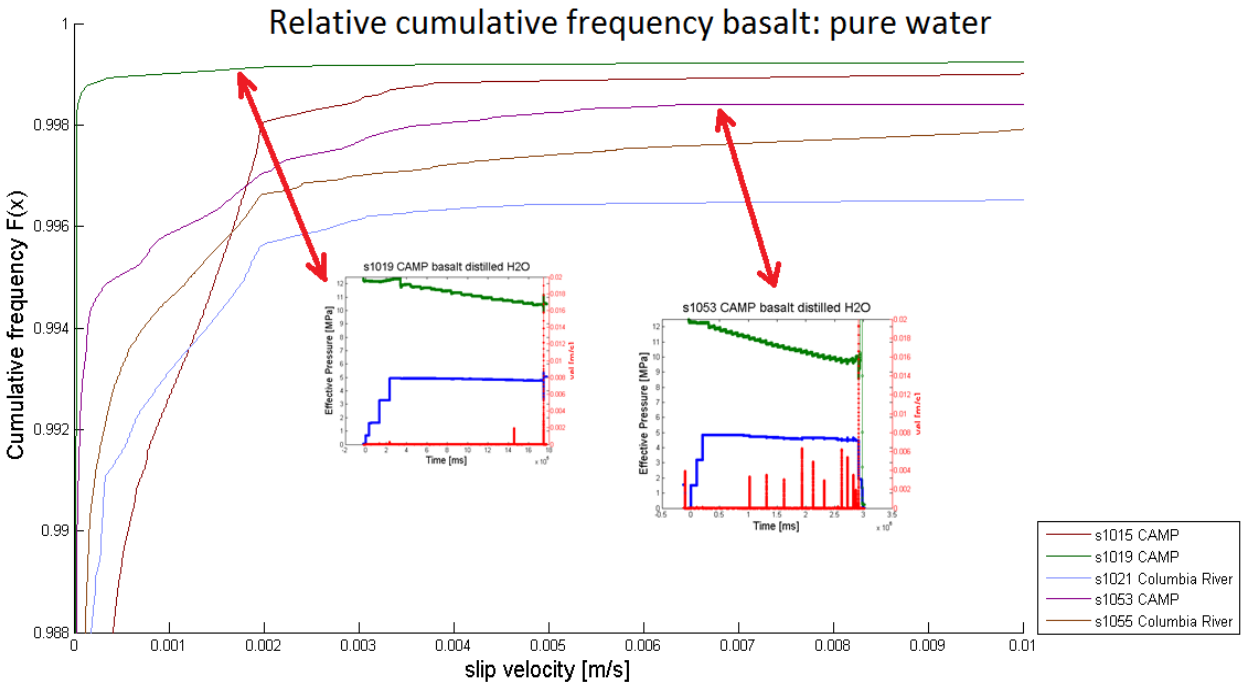

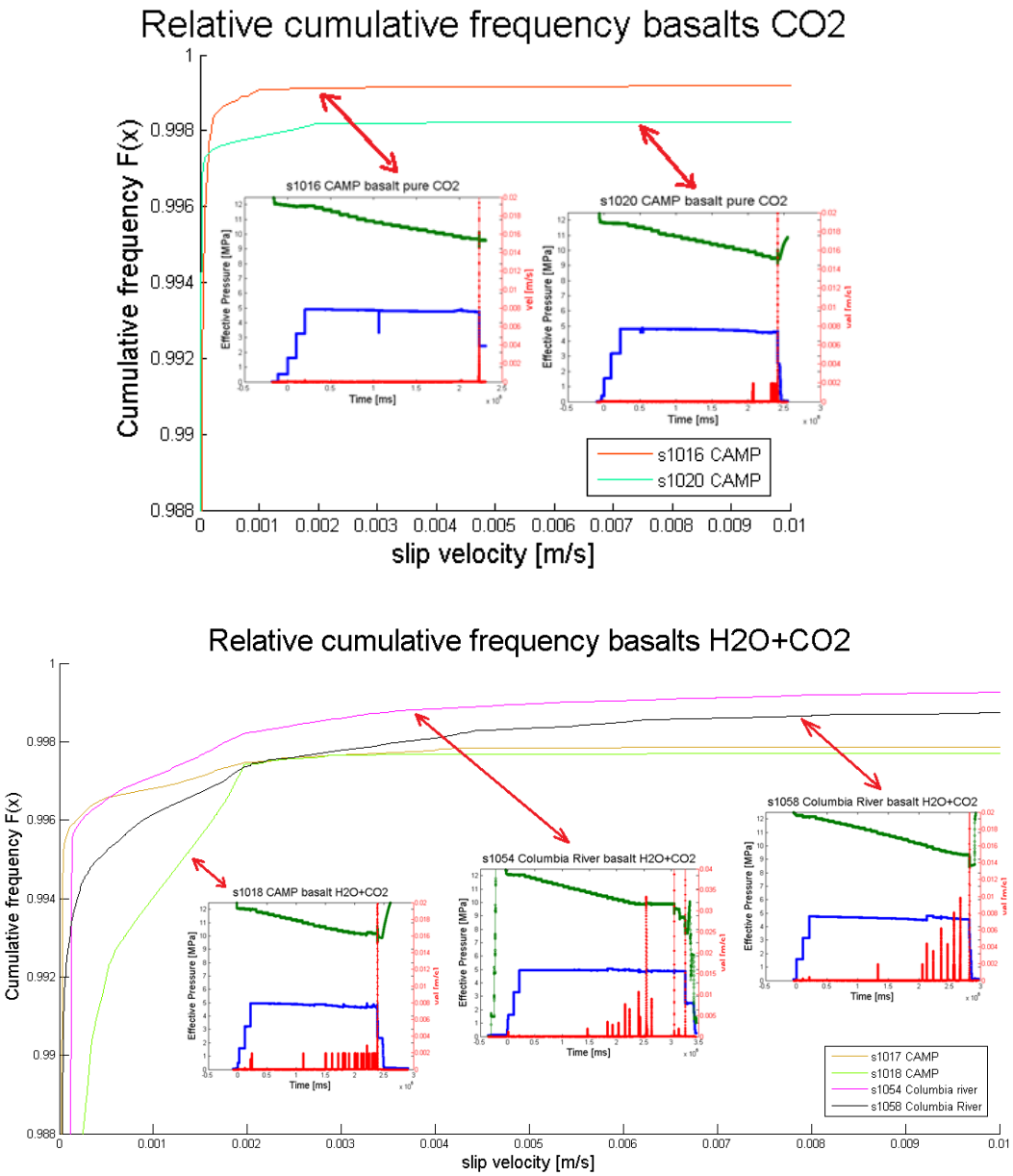

Figure 22: *Relative cumulative frequency curve in basalts with insets of precursory events recorded during the tests with a) pure H_2O, b)pure CO_2, c)H_2O+CO_2 mixtures*

We notice from figure 22 the different evolution of cumulative frequency lines:

for example in the first plot with pure H_2O, s1019 curve is very steep because all precursory events are concentered in what we defined as background noise, whereas s1053 exhibits a curve whose relative frequency values continue to grow even at slip velocity greater than 0.002 m/s. This is confirmed by the occurrence of precursory

events with slip velocity greater than 0.002m/s (inset s1053 linked to s1053 curve). The same way of thinking can be extended to pure CO_2 and H_2O+CO_2 plots.

In pure CO_2 experiments, s1020 has a greater number of events with v=0.002 m/s compared to s1016, whose number of precursory events is really low. This translates into a steeper frequency distribution curve in s1016 that reaches its plateau starting from v =0.001 m/s and in a smoother curve in s 1020.

Instead, H_2O+CO_2 tests s1017 and s1018 show instability events with values around 0.001 m/s and 0.002 m/s and the latter exhibits higher frequency events, whereas s1054 and 1058 curves show instability events with higher slip velocity values and higher occurrence frequencies.

s1054 and s1058 show similar cumulative frequency; in fact if we look at their mechanical data, they are alike both regarding the number of preceding events but even concerning slip velocity value reached during those events.

Hence, cumulative frequency is a very useful tool to compare in a simple and immediate way, preceding events distribution among the different experiments.

Experiment	**Fluid involved**	**Number of events >0.001 m/s (excluding main instability event)**	**Effective pressure corresponding to the 1st precursory event [MPa]**	**Peak of slip [m]**
s1015	Tap water	43	10.9	0.031
s1019	Distilled H_2O	1	10.8	0.018
s1021	Distilled H_2O	10	10.7	0.039
s1053	Distilled H_2O	13	11.5	0.035
s1055	Distilled H_2O	22	10.0	0.060

s1016	Pure CO_2	0	/	0.013
s1020	Pure CO_2	5	9.4	0.022
s1017	H_2O+CO_2	1	10.4	0.008
s1018	H_2O+CO_2	45	12.0	0.034
s1054	H_2O+CO_2	13	10.8	0.095
s1058	H_2O+CO_2	10	11.1	0.043

***Table 8**: Preceding events counting and effective pressure corresponding to the 1st precursory event for experiments with basalts*

Table 8 highlights a great variation of number of events even in experiments conducted with the same fluid. However, combining the information of this table with the previous plots we can observe three families grouped according to number of events, occurrence of 1st precursory event and the deferral of these events in time:

1)s1016, s1020, s1017 and s1019 family , characterized by a low number of precursory events and the first event occurred at an effective pressure between 9.4 and 10.4 MPa;

2) an intermediate family (s1054, s1058, s1021 and s1055) with ~ 15-20 preceding events spaced in time (every 100-200 sec). The first event occurrence corresponds to a normal effective stress of ~ 11 MPa;

3) the other end member s1015 and 1018 group, distinguished by the other two for its greater number of preceding events (~40) very close one to the others in terms of time, in particular with main instability approaching.

3.1.3.1 Precursory events: Carrara marbles

The same statistical analysis was applied to Carrara marble experiments. We can see from figure 22 and table 9 that s1052 (pure H_2O) has only two significant precursory events. Once again low occurrence frequency reflects in a very steep cumulative frequency curve.

Instead s1056 and s1057 show the first precursory event when first shear step was applied (corresponding to 12.5 MPa effective pressure). These precursory events have a slip velocity of approximately 0.002 m/s (in fact if we look at the relative frequency distribution, curve plateau is reached at that value) and the frequency of slip "burst" events increases in time approaching the main instability.

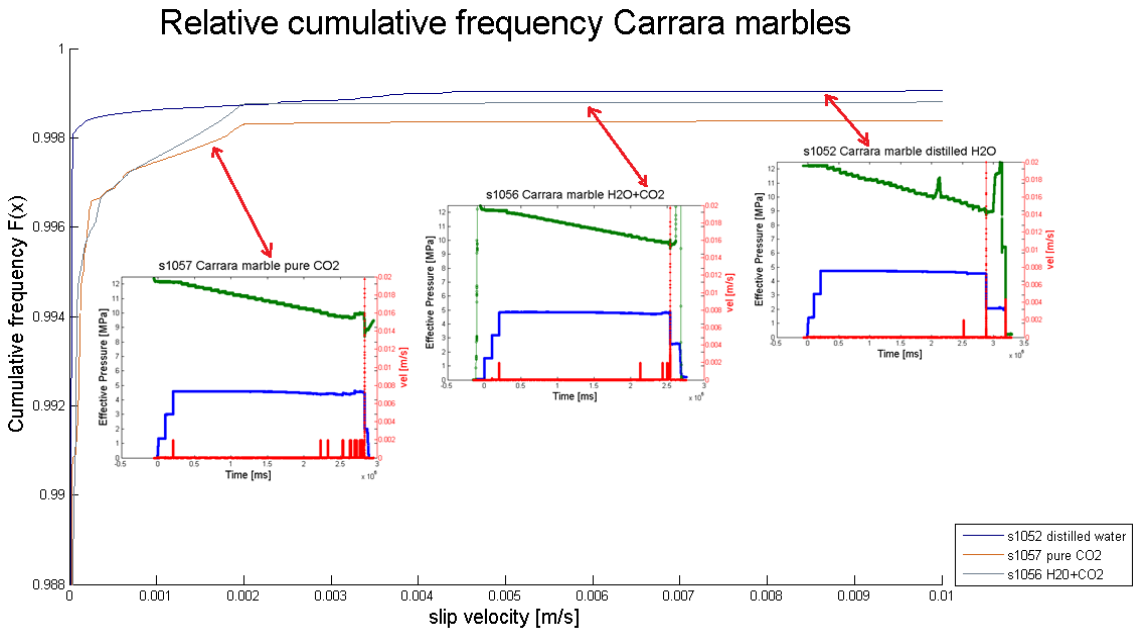

Figure 23: *Relative cumulative frequency curve in Carrara marbles with insets of precursory events recorded during the tests with a) distilled H_2O, b)pure CO_2, c)H_2O+CO_2 mixtures*

Experiment	Fluid Involved	Number of events >0.001 m/s (excluding main instability event)	Effective pressure corresponding to the 1st precursory event [MPa]
s1052	Distilled H_2O	2	9.6
s1057	Pure CO_2	16	12.2
s1056	H_2O+CO_2	11	12.2

***Table 9**: Preceding events counting and effective pressure corresponding to the 1st precursory event for experiments with Carrara marbles*

3.1.4 LVDT & DCDT data

Axial shortening measurements were performed with high resolution LVDT & low resolution DCDT. These data are necessary to quantify the amount of rock wear.

Both devices work thanks to Faraday-Neumann-Lenz's law: a ferromagnetic core slips through a coil which induces a concatenated magnetic flow which in turn induces an electric voltage, whose sign opposes to the cause that generated it. So, we have positive sign if the core slips away from the inducer, vice versa if the core slips towards it.

Figure 24 shows axial shortening as a function of time and slip.

In fig. 24a we notice a progressive increase in shortening with time during the tests. This gradual increase is strictly related to pore pressure steps, as documented in figure 24c. During the onset of instability remarkable shortening occurs (in figure 24 shortening occurred in this phase is ∼70 % of total shortening), but after ∼ 100 ms the onset, when slip velocity starts to oscillate during main instability, we observe an oscillatory response for the LVDT as well. We speculate that this might be caused by a misalignment of the pair rock samples.

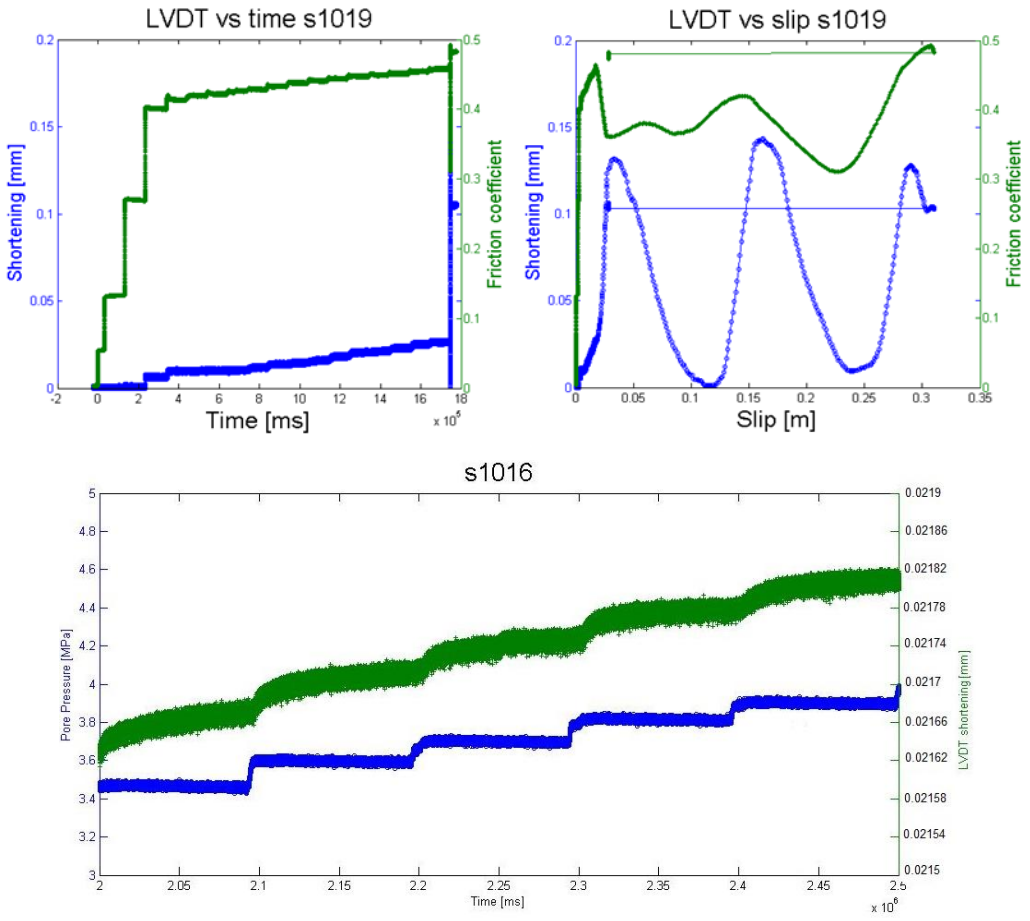

Fig24: *Axial shortening evolution with time (a) and slip (b). During the test axial shortening is strictly related to pore pressure increase (c)*

From test s1052 to s1058 we used low resolution DCVT due to the LVDT failure. In this case we had to smooth the recorded signal. Smoothing consists of calculating the mean of a specified number of points in order to obtain a cleaner data. In our case, smoothing was set to 1000 (note that sample acquisition rate was of 250 Hz).

Similarly with previous results, we listed in tables 10 and 11 the peak of shortening prior to the main instability for each experiment, whereas we did not plot shortening per unit of slip due to shortening oscillation during main instability.

3.1.4.1 LVDT & DCVT data: basalts

Table 10: *List of shortening prior instability (peak of shortening) in basalts*

Experiment	Fluid involved	Peak of shortening [mm]
s1015	Tap water	0.012
s1019	Distilled H_2O	0.027
s1021	Distilled H_2O	0.045
s1053	Distilled H_2O	-0.004
s1055	Distilled H_2O	0.060
s1016	Pure CO_2	0.067
s1020	Pure CO_2	0.007
s1017	H_2O+CO_2	-0.114
s1018	H_2O+CO_2	0.019
s1054	H_2O+CO_2	-0.003
s1058	H_2O+CO_2	0.022

Peak of shortening ranges from 0.007 to 0.060 mm. In H_2O and CO_2 experiments rock cover all this range, instead in H_2O+CO_2 experiment this interval is narrower. Experiments with negative values are not comparable with the others. In fact in s1017 shortening data are spurious probably because of a numerical problem (first type discontinuity before the main instability), in s1053 signal is almost flat around the 0, whereas in s1054 shortening may be caused by the decrease of 0.5 MPa in normal stress, as suggested by figure 13. For this reason the peak of shortening value in s1058 may have been undervalued.

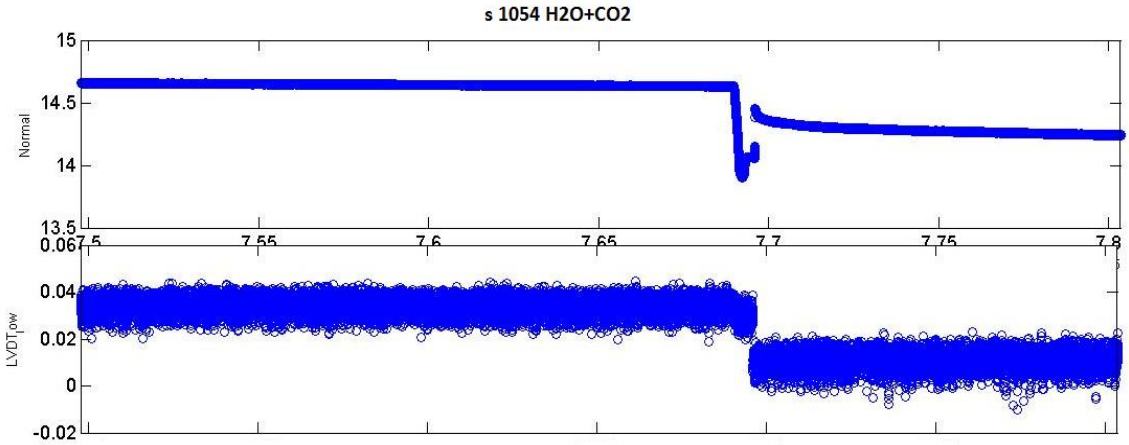

***Figure 25**: Negative shortening in s1054 due to normal stress decrease*

3.1.4.2 LVDT & DCVT data: Carrara marbles

The same procedure was done for Carrara marbles.

***Table 11:** List of shortening prior instability (peak of shortening) in basalts*

Experiment	Fluid involved	Peak of shortening [mm]
s1052	Distilled H_2O	0.011
s1057	Pure CO_2	0.015
s1056	H_2O+CO_2	0.021

In Carrara marbles the peak of shortening varies from 0.011 to 0.021 mm. Shortening data are similar, even though they are too few to make sound statements from a statistical point of view.

3.2: Microanalytical data

3.2.1:Basalts

In the presence of pore fluids most of the fine grained gouge material produced during sliding was flushed away with the fluid when the valves were opened at the end of the experiment.

Nevertheless, it was possible to investigate if a transition in mineralogy, grain size and microstructure occurred from the host rock to the slip zone after fluid-rock interaction during the experiment.

For this purpose, seven post-experimental rock cylinders from the stationary side (AN 116-s1016, AN 103-s1017, AN 118-s1018, AN 116-s1019, AN 127-s1020, CR 1-s1054, CR 2-s1058) were cut perpendicular to the sliding surface and tangentially to the slickenlines (formed due to the abrasive wearing during the experiments) as shown in figure 26 and then analysed at the optical microscope. Instead, the sliding surface of four rock samples from rotary side (NEW37-s1016, AN 116-s1017, AN 62- s1018, AN 103-s1019) was investigated with Raman spectroscopy analysis.

All analysis were performed with a monochromatic green light (580 nm wavelength).

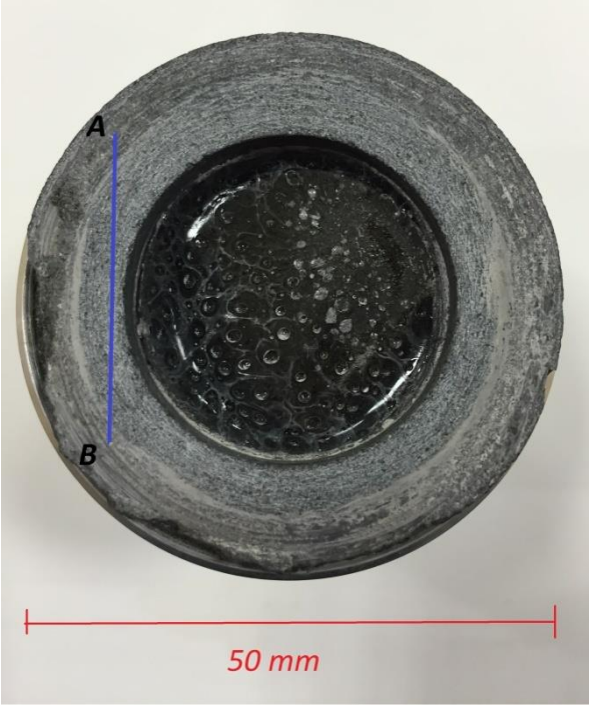

***Figure26**:Example of a post-experimental rock sample before the cutting tangentially to the slickenlines and perpendicular to the sliding surface (cross section A-B).*

Under the optical microscope, we did not find any evidence of fluid-rock interaction: all post-experimental samples preserved the same microstructures and mineralogy of the un-deformed rocks (see section 2.3).

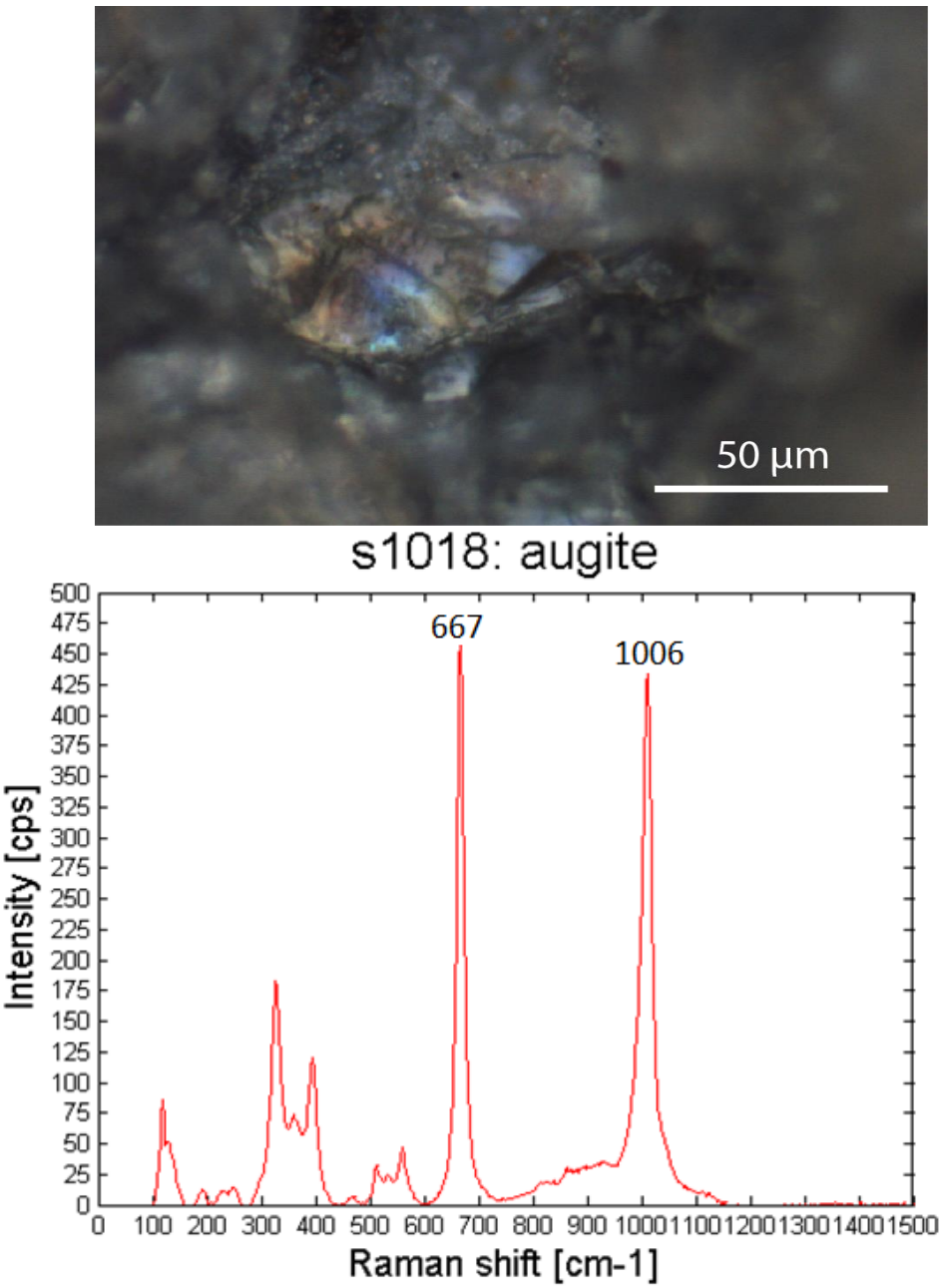

Figure 27 **a**: augite crystal observed at the Raman binocular; **b:** Raman spectrum of augite with its characteristic peak at 667 and 1006 cm^{-1}

However, when in Raman-spectroscopy analysis we focused on the gauge formed on the sliding surface, together with the "basaltic" minerals (plagioclase, olivine and augite, e.g, figure 27), in the case of the CAMP basalts sheared in the presence of H_2O+CO_2 fluid (s1017,s1018) we also identified crystals of calcite and dolomite (calcite and dolomite main peaks are located at 1087 and 1097 cm^{-1}, respectively: figures 28a, 29a:).Calcite and dolomite were absent in the undeformed rock.

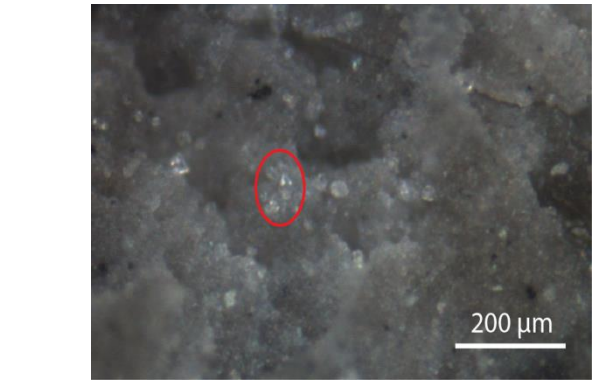

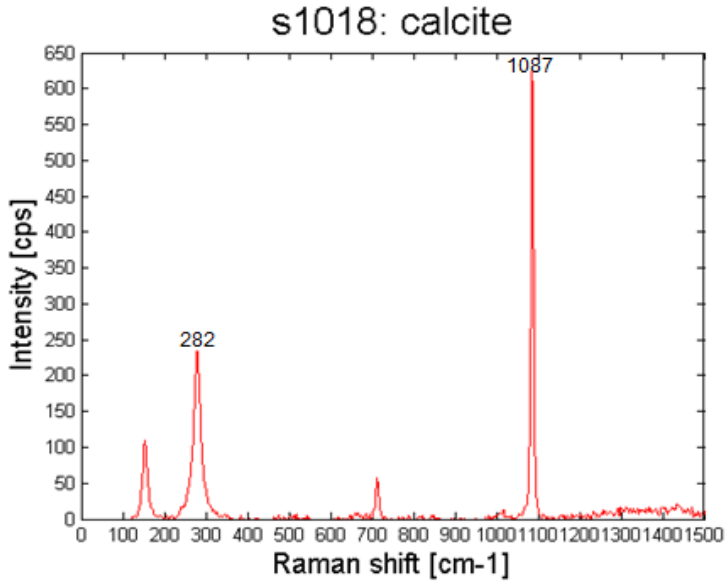

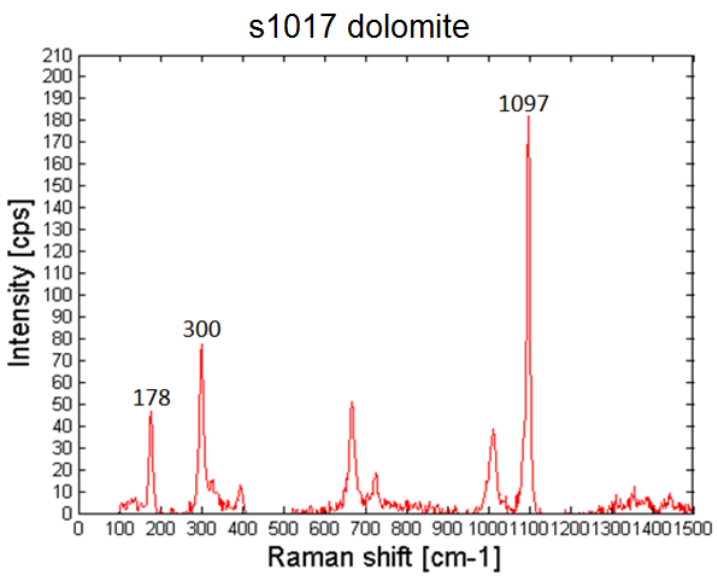

At the top of the panel. ***Figure 28: a*** *calcite and* ***b*** *dolomite crystal found in CAMP basalt during H_2O+CO_2 experiment.*
At the bottom, ***figure 29:*** *Raman spectra of the selected* ***a*** *calcite and* ***b*** *dolomite with the most characteristic peaks of the mineral phase.*

3.3: Chemical data

3.3.1:Fluid analysis after the experiments

The enrichment in major elements in the fluids collected after the H_2O and H_2O+CO_2 experiments are reported in Table 12 and Fig. 30.

The total volume of fluid collected resulted from the different volume of fluid involved in each experiment. The difference was caused by:

a. The configuration of the pressurizing system during pure water and H_2O+CO_2 mixtures experiments (see 2.1.2.1 for details);
b. The volume of the central hole that varied from one sample to another due to sample preparation, i.e. the different height of the inner solid rock cylinder and the amount of epoxy used to seal the sample.
c. Fluid leakage during and after the experiments: for instance, during experiments s1015 and s1017, fluids were collected with a panpipe, with large fluid loss. For this reason it was not possible to perform fluid analysis in those two experiments.

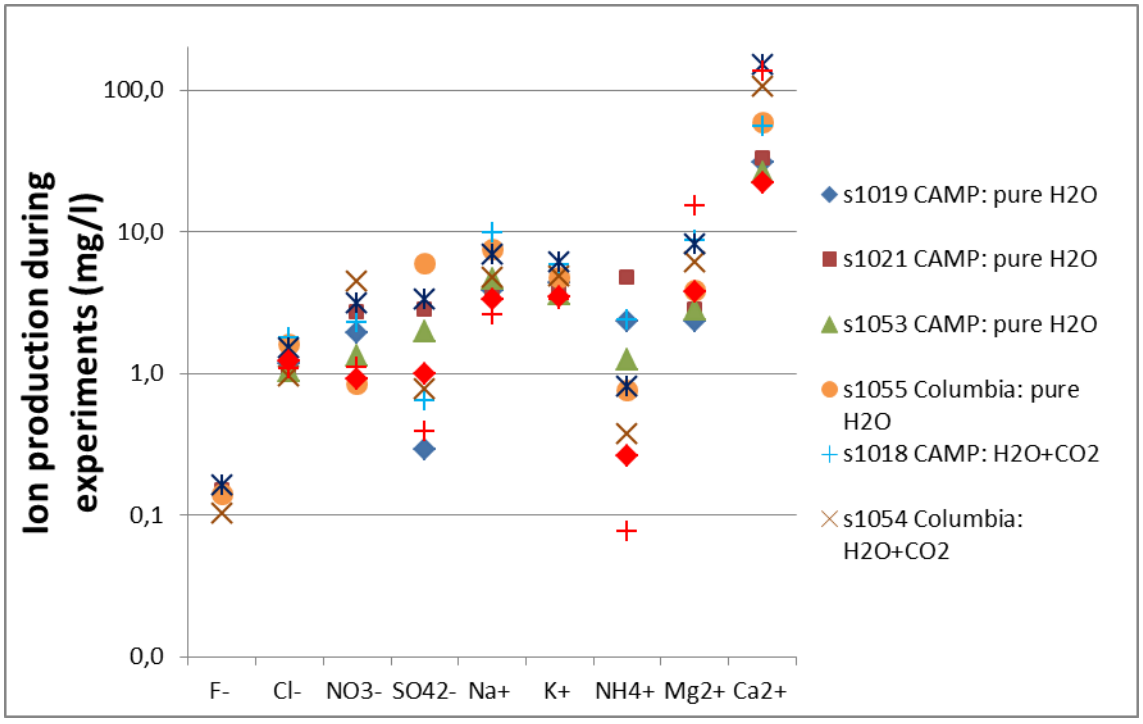

Figure 30: *Composition of the pore fluid after the experiments*

3.3.1.1:Fluid analysis after the experiments: basalts

Anions: nitrate and sulphates ions content is similar in all the experiments, varying from 0.3 to 6 mg/l. Columbia River basalt has (on average) an higher content of these cations.

Cl^- concentration is ~ 1 mg/l in all the experiments; fluorine ion is absent in some fluid interacted with CAMP basalts.

Cations: Alkaline cations content is rather similar in both H_2O and H_2O+CO_2 experiments: Na^+ content ranges between ~4 and 10 mg/l, whereas $[K^+]$ is slightly lower (3-6 mg/l).

Mg^{2+} concentration is strongly affected by the type of fluid involved: in H_2O-rich experiments, Mg^{2+} concentration is ~ 3 mg/l, whereas in H_2O+CO_2 experiments is ~6 mg/l. The same applies to Ca^{2+} concentration: in H_2O-rich fluids Ca^{2+} concentration is ~ 30-50 mg/l, instead in H_2O+CO_2 experiments Ca^{2+} concentration is between 50 and 150 mg/l.

We observed that this content is on average higher in Columbia River compared to CAMP basalts, in contrast to ammonium ion content (2-4 mg/l in CAMP basalts VS 0.3-0.8 mg/l in Columbia River basalts).

3.3.1.2: Fluid analysis after the experiments: Carrara Marbles

Anions: Chloride, sulphates and nitrate ions are within the anions content range of fluids interacted with CAMP basalt. Hence, it is not dependent on the starting fluid composition (H_2O or $H_2O+ CO_2$). Determination of HCO_3^- content was possible just in s1052 because the minimum volume of fluid required for this analysis was 50 ml. Cl^- concentration is ~ 1 mg/l in all experiments, whereas fluorine ion is absent.

Cations: The behaviour described in anions also applies to Na^+ and K^+. Instead, Ca^{2+} and Mg^{2+} concentration is ~ 5 times higher in CO_2-H_2O mixtures than in H_2O pure fluids:

Ca^{2+}concentration is 22 mg/l in H_2O experiments and 135 mg/l in H_2O+CO_2 tests; Mg^{2+} is ~ 4 mg/l in H_2O-rich fluids and 15 mg/l in H_2O+CO_2 mixtures. Ammonium content is slightly lower than in the fluids collected in the experiments conducted with the Columbia River basalts (<0.3 mg/l).

Table 12. Pore fluid experiments: ion composition of fluids collected after the experiments . The chemical composition of fluids was determined by ion chromatography (see Methods, section 2.2.4). The relationship between chemical data and total cumulated slip will be discussed in 4.2.3

Test	Sample	Fluid used during the tests	Volume collected after experiments (ml)	Total cumulated slip (m)	F^- (mg/l)	Cl^- (mg/l)	Br^- (mg/l)	NO_3^- (mg/l)	SO_4^{2-} (mg/l)	HCO_3^- (mg/l)	Na^+ (mg/l)	K^+ (mg/l)	Mg^{2+} (mg/l)	Ca^{2+} (mg/l)	NH_4^+ (mg/l)
s1019	CAMP basalt	distilled H2O	4,0	0.31	/	1,2	< 0.01	1,9	0,29	/	3,8	4,3	2,3	31	2,3
s1021	CAMP basalt	distilled H2O	8,0	2.30	0,15	1,1	< 0.01	2,7	2,8	/	3,8	3,7	2,8	33	4,8
s1053	CAMP basalt	distilled H2O	14,5	1.38	/	1,0	< 0.01	1,3	2,0	/	4,6	3,6	2,8	26	1,3
s1055	Columbia River basalt	distilled H2O	14,5	1.00	0,14	1,6	< 0.01	0,83	6,0	/	7,4	4,7	3,9	59	0,75
s1018	CAMP basalt	mixture H2O+CO2	22,0	0.26	/	1,8	< 0.01	2,3	0,64	/	9,9	5,8	8,7	55	2,4
s1054	Columbia River basalt	mixture H2O+CO2	5,0	0.50	0,10	0,94	< 0.01	4,4	0,78	/	4,8	4,8	6,0	105	0,37
s1058	Columbia River basalt	mixture H2O+CO2	10,5	1.15	0,16	1,5	< 0.01	3,1	3,3	/	6,9	6,0	8,1	152	0,80
s1052	Carrara marble	distilled H2O	78,0	0.85	/	1,2	< 0.01	0,91	1,0	104	3,3	3,5	3,8	22	0,26
s1056	Carrara marble	mixture H2O+CO2	12,5	1.21	/	1,1	< 0.01	1,1	0,39	/	2,6	3,3	15	135	0,08
H20 Roma 12/11/14					0,35	6,2	< 0.01	7,1	9,6	287	15	15	18	46	0,26

3.4: Temperature measurements and estimates

3.4.1: Temperature measurements

During the experiments we conventionally fixed the reference initial temperature to 23°C, because the mean room temperature during our tests was about 25°C, and it is reasonable to assume that the steel of the pressure vessel was slightly colder than the air. The initial temperature correspond to instant t ranging from 170-2000 s before the instant t0 (for definition of t0, see section). The thermocouple was installed starting from experiment s1017.

Basalts

In most experiments, independently of the type of fluid, temperature increased abruptly of 0.5-1.5°C during the main instability events. Moreover, in pure CO_2 fluid, an increase in temperature of ~ 0.1-0.5 °C occurred also during the stepwise increases in 0.1 MPa pore pressure, due to the exothermal gas expansion travelling from the cylinder (~ 5 MPa) to the vessel (corresponding to 2.5 MPa at t0); the overall evolution of the temperature with time showed a decreasing trend (~0.3 MPa). Instead, in H_2O distilled fluid experiments temperature was not sensitive to fluid pressure variations, except during main instability events (fig.31a).

H_2O+CO_2 experiments showed a transitional behaviour between pure H_2O and pure CO_2 end members: in some cases their temperature variation with time was the same as pure CO_2 experiments. In other experiments their response with increasing pressure was absent as reported in the case of distilled H_2O experiments. In the case of H_2O+CO_2 the strong variability of the temperature to a pressure change is attributable to the competition between the CO_2 diffusion time inside the vessel and the rate of increase of CO_2 which was regulated manually.

Excluding the CO_2 fluid experiments, the overall temperature evolution with time is rather difficult to interpret: in fact, if we just consider the H_2O fluid experiments, the temperature may either increase, decrease or keep a stationary trend with time.

Carrara marbles

Temperature evolution in Carrara marbles was similar as in basalts: in all the experiments (H_2O, CO_2, H_2O+CO_2) was measured a pulse in temperature of about 1-1.5°C during the main instability and only in CO_2 experiments was measured a small temperature pulse (~0.25°C) during the stepwise pore pressure increase (figures 31b,c).

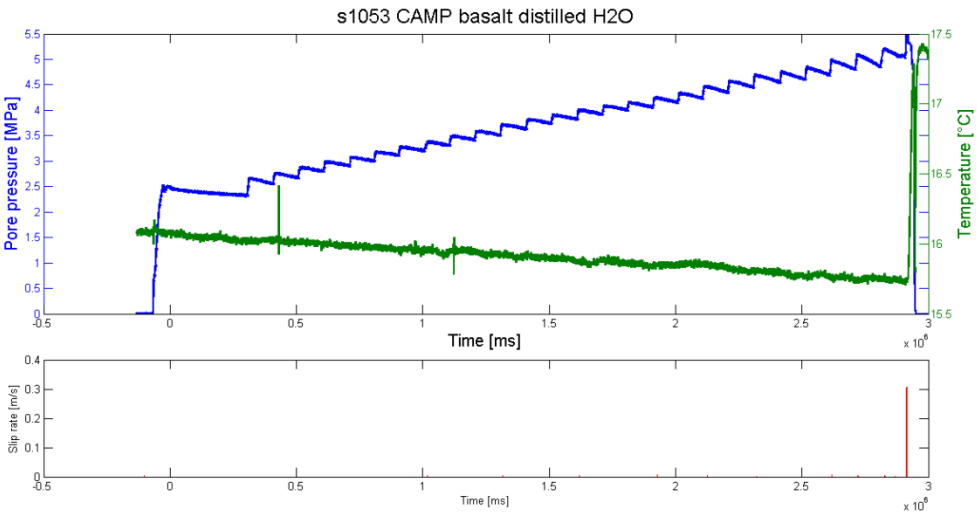

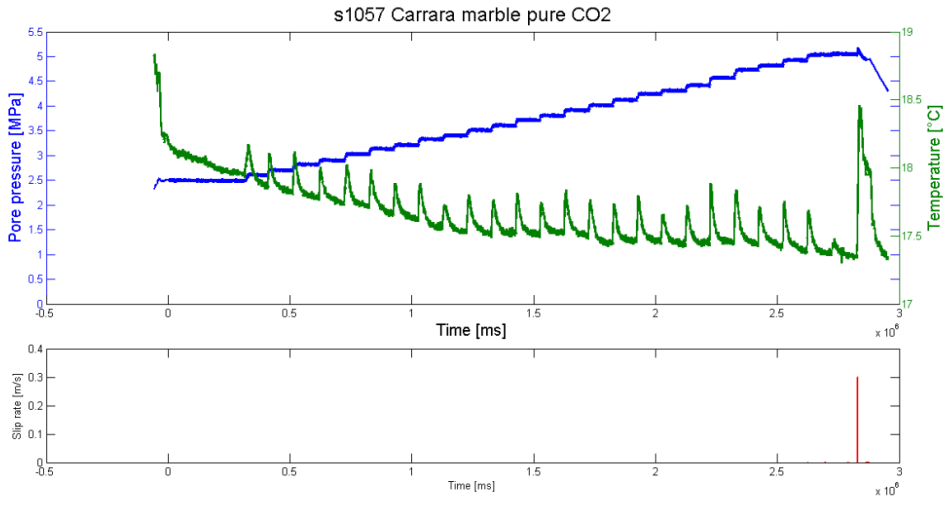

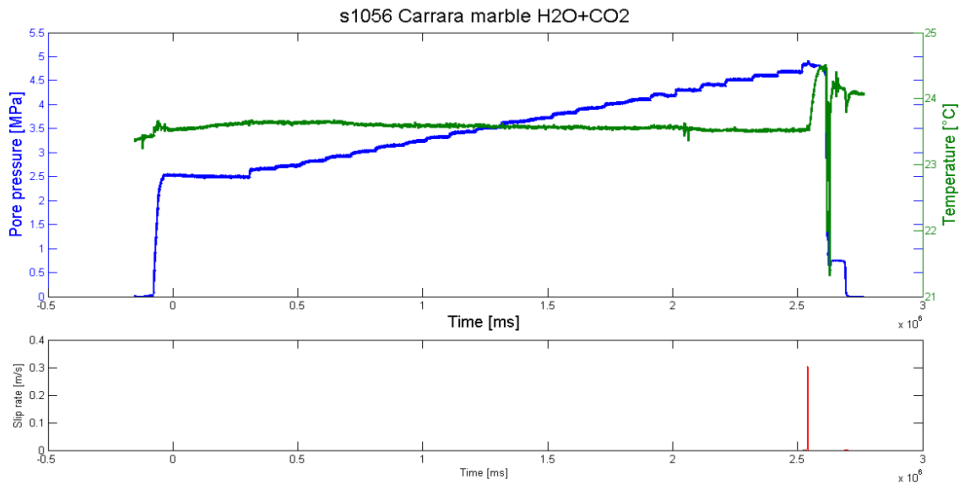

Figure 31: *Temperature and pore pressure evolution with time In basalts and Carrara marbles for* ***a:*** *distilled H_2O,* ***b:****pure CO_2 and* ***c:*** *H_2O+CO_2 experiments. In the bottom panel we plotted slip rate as a function of time to highlight instabilities events*

3.4.2: Temperature estimates

We estimated the temperature transferred from the slipping zone to the water in accordance with Eq.7:

$$T_f(i) = T_{room} + \frac{\frac{1}{\rho \cdot Cp \cdot \sqrt{\kappa\pi}} \cdot \int_0^t \frac{1}{2} \cdot \frac{\tau(t') \cdot V(t')}{\sqrt{t-t'}} dt}{c_w \cdot \rho_w} \qquad \text{Eq.7}$$

using the experimentally-measured heat production rate per unit area (product of τ and V) in each instant t_i, with the thermal diffusivity κ=0.0121 cm^2/s, Hanley et al.,1978), the thermal capacity of basalt Cp = 900 J/Kg/K (at 300 K, Waples & Waples, 2004), the thermal capacity of water Cw = 4183J/Kg/k (at 300 k), the rock density ρ =2960 Kg/m^3 (data for non-porous basalts) and the water density ρ_w =999.97 Kg/m^3. We assumed room temperature T_{room} equal to 23 °C for each experiment.

In table 13 are reported the maximum temperatures estimated in the slipping zone from Eq. 7 and the temperatures measured with the thermocouple at the instant t_{peak} corresponding to the maximum temperature estimate. Obviously, the temperature increase estimated by means of Eq. 7 is higher than the one measured by the thermocouple inside the vessel because (1) Eq. 7 assumes a slipping zone of zero thickness, whereas the gouge layer has a thickness of few tens of micrometers at least and (2) the thermocouple is not located on the sliding surface. The maximum temperature estimated is achieved few seconds (~4-5 s) after the peak in shear stress leading to the main instability, once the sample was accelerated and slipped for few mm-cm. Since the maximum temperature achieved in the slip surface is proportional to the heat rate production (and thus to V), we infer that the maximum temperature was achieved during the main instability event, even in the case of experiments that do not have a temperature increase detected by the thermocouple.

***Table 13**: Comparisons between the maximum temperature estimated in the slipping zone and the temperature measured with the thermocouple at the same instant t.*

Test	Sample	Fluid involved	T estimated (slip zone) [°C]	T measured [°C]	Slip corresponding to T est [m]	Peak of slip [m]	Time corresponding to T estimated [ms]	Time corresponding to peak parameters [ms]
S1019	CAMP	Distilled H_2O	39.4	23.2	0.029	0.018	1747044	1745192
S1021	CAMP	Distilled H_2O	92.9	18.0	0.047	0.039	2410396	2402000
S1053	CAMP	Distilled H_2O	61.7	15.7	0.043	0.035	2917732	2912316
S1055	Columbia	Distilled H_2O	57.6	23.4	0.070	0.060	2135480	2131460
S1020	CAMP	Pure CO_2	60.6	22.7	0.042	0.022	2410348	2405544
S1017	CAMP	H_2O+CO_2	59.9	23.3	0.015	0.008	1441564	1437496
S1018	CAMP	H_2O+CO_2	29.4	23.8	0.232	0.034	2391436	2386312
S1054	Columbia	H_2O+CO_2	41.0	17.7	0.100	0.095	3255164	3252636
S1058	Columbia	H_2O+CO_2	63.0	20.1	0.050	0.043	2825640	2821416
S1052	Carrara	H_2O	49.6	15.0	0.022	0.015	2886752	2882912
S1057	Carrara	CO_2	49.4	17.9	0.092	0.020	2831372	2827620
S1056	Carrara	H_2O+CO_2	62.5	23.6	0.030	0.021	2542400	2537556

4.Discussion

4.1:Basalts and interaction with H_2O- and CO_2- rich fluids

4.1.1:Mechanical data

4.1.1.1:Main instability events

In all the environmental conditions investigated (pure H_2O, pure CO_2 and H_2O+CO_2 fluids) the peak effective friction, $\mu_{p,eff}$ ranged from 0.45 to 0.6. The value of pore pressure reached before the main instability ranged from ~4 to 6 MPa, approaching gradually hydrostatic conditions (i.e. the ratio between pore pressure and normal stress tends to 0.4). Figure 32 shows a linear trend of the frictional evolution with normal effective pressure, as described by equation 4.

According to our data-set, Columbia River basalts had the main instability at lower effective stress (= higher pore fluid pressure) than CAMP basalts (Fig. 32). The frictional strength of an experimental fault is controlled by the combination of the chemical composition of the fluid involved, the geochemistry (and thus mineralogy) of the sheared samples and their grain size, as follows.

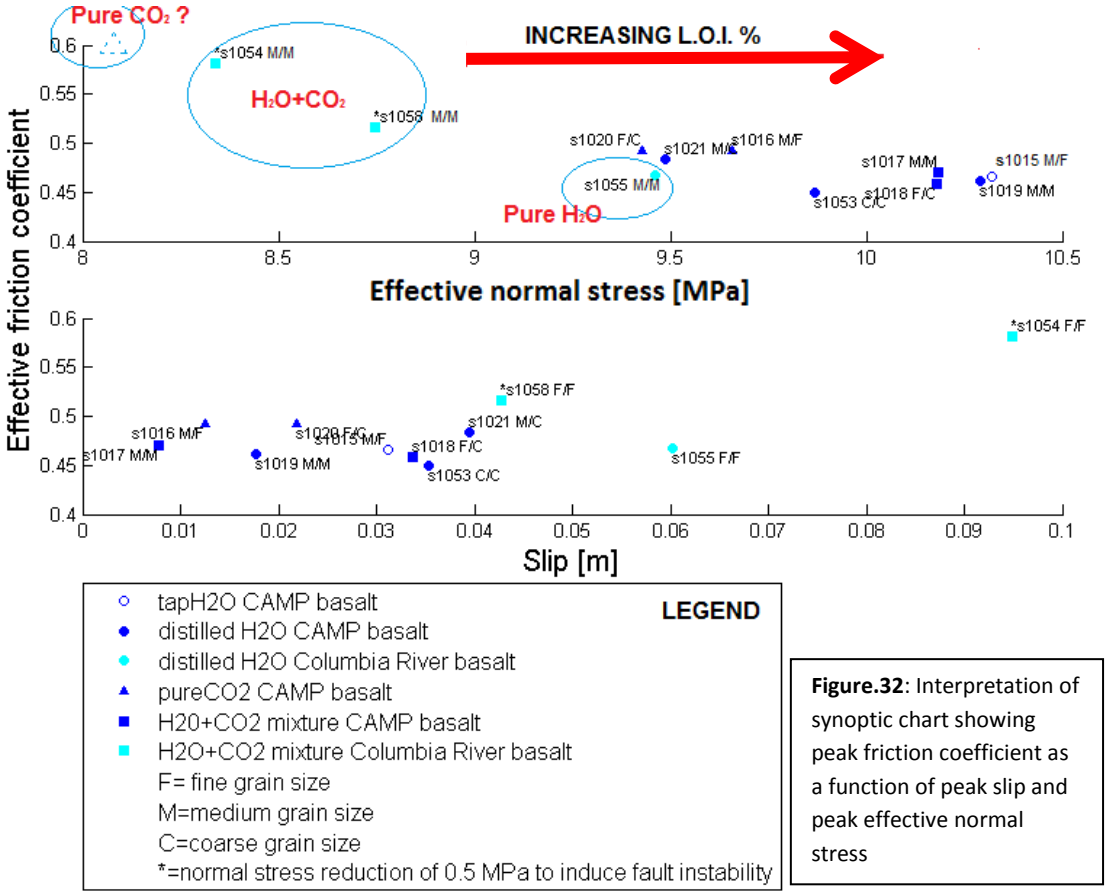

Figure.32: Interpretation of synoptic chart showing peak friction coefficient as a function of peak slip and peak effective normal stress

Role of Mineralogy

In both CAMP and Columbia River basalts, primary mineral constituents are similar: plagioclase, augite and Fe-Ti oxides. Hence, micro-indentation hardness σ_y should be similar in both rocks. The only difference between the two rocks consists in the presence of small amounts of olivine and alkali-feldspar in Columbia River basalts. However, since the Mohs hardness H_m of olivine and K-feldspar is 6, same as at that of plagioclase and pigeonite-augite, and the σ_y is: (Broz et al., 2006)

$$\sigma_y = 0.123\ H_m^{2.3} \qquad \text{Eq.8}$$

we conclude that all the global mineral assemblage in both basalt groups is expected to have similar σ_y.

One notable difference between the basalt groups is however the widespread presence of secondary alteration minerals in the analyzed CAMP basalts, while the Columbia samples are generally fresh (i.e. contain primary magmatic minerals, mostly).

According to my interpretation, a key factor in controlling the peak friction (or the friction associated to the main instability, Fig. 32) is the presence of alteration minerals which might lower the shear strength and thus the peak ("static") friction of rocks (Byerlee, 1978). According to optical analysis of thin sections and chemical and mineralogical analysis (XRF and XRPD, Table 14) of the rock powders, CAMP basalts are on average significantly more altered than Columbia River basalts. In fact, L.O.I. (loss on ignition) values are on average higher in CAMP (~1.5-2 wt.%) than in Columbia River basalts (1.0 wt.%). Higher L.O.I. values in CAMP rocks are related to higher amounts of alteration minerals such as smectite, chlorite, sericite and illite from devitrification of sideromelane basaltic glass and from the alteration of olivine and pyroxenes (smectites and chlorites) and of plagioclase (sericite and illite). Thus, the amount of clay mineral seems to lower the peak effective friction coefficient and thus the effective normal stress at which fault reactivation occurs.

Therefore, it is reasonable to divide the top panel of figure 32 in CAMP and Columbia regions. Their boundary is located at ~0.5 effective friction corresponding to ~ 9.4 MPa effective normal stress.

Role of Fluid composition

It is easier to interpret the role of fluid composition by subdividing figure 32 into CAMP and Columbia River regions. In the case of the CAMP basalts with the same grain size and mineralogy, the experimental fault reactivates at higher effective normal stress in H_2O-rich fluids than in H_2O+CO_2 mixtures, and, at further lower effective normal stresses, in pure CO_2 fluids.

Note that in CAMP basalts experiments s1021 and s1053 performed in distilled H_2O, the instability occurred at lower effective normal stress because of their lower alteration rate (1.69% vs 2.25%, Table 14) compared to the other CAMP samples (>2%, Table 14) sheared in the experiments. Hence, we speculate that a hypothetical experiment in

the presence of pressurized CO_2 with Columbia River basalts characterized by the same grain size as the other Columbia experiments, would fail at lower normal effective pressures than in H_2O+CO_2 experiments (figure 32).

Moreover, s1021 (CAMP basalt) is less altered than s1053 (CAMP basalt) but has similar alteration (1.69 wt.% LOI) as s1055 (Columbia river, 1.86 LOI: see XRF, table 14), explaining why the effective normal stress at peak friction of s1021 almost overlaps with the one of s1055. However in s1021 test a problem occurred at ~ 300-450s (corresponding to 2.7 MPa): the sample holder from the rotary side rotated and this might have modified the permeability (e.g. due to gouge production). This might affect the Biot factor assumed as equal to 1 in eq.4: a smaller Biot factor would result in a higher effective normal stress than the one reported in Fig. 32.

Experiment	Pair sample		Grain size	Fluid involved	LOI %	Sum LOI %
S1015	AN116	NEW37	M/F	Tap water	2,66-0,25	2,91
S1016	AN116	NEW37	M/F	Pure CO_2	2,66-0,25	2,91
S1017	AB103	AN116	M/M	H_2O+CO_2	0,81-2,66	3,47
S1018	AN118	AN62	F/C	H_2O+CO_2	2,75-0,37	3,12
S1019	AN116	AN103	M/M	Distilled H_2O	2,66-0,81	3,47
S1020	AN127	NEW50	F/C	Pure CO_2	2,15-0,55	2,7
S1021	AN140	AN62	M/C	Distilled H_2O	1,32-0,37	1,69
S1053	NEW70	NEW50	C/C	Distilled H_2O	1,70-0,55	2,25
S1054	CR1	CR2	M/M	H_2O+CO_2	0,90-0,93	1,83
S1055	CR2	CR2	M/M	Distilled H_2O	0,93-0,93	1,96
S1058	CR2	CR1	M/M	H_2O+CO_2	0,93-0,90	1,83

Table 14 : Loss of ignition (1000°C) in basaltic pair samples: Columbia River are generally less altered than CAMP basalts

Role of Grain size:

In general, all the investigated rocks are fine grained volcanic rocks. All the experiments show different degrees of alteration, complicating the investigation of the role of grain size. Furthermore, each basalt group (Columbia River vs CAMP) showed a difference in grain size distribution depending on rock microtexture: grains in doleritic basalts (coarse grain size in Figure 32) and in microporphyric basalts (fine grain size in Figure 32) have similar dimensions, whereas porphyric basalts (medium grain size in Figure 32) have phenocrysts drowned in a fine grained matrix, therefore with a more heterogeneous particle size distribution. But even in rocks with similar grain-size, mineral shapes are different: e.g. plagioclase usually shows an elongated prismatic or acicular shape, while pyroxens are more rounded and squat. Hence, for all these reasons, it is challenging to find a correlation between grain size distribution and peak friction.

4.1.1.2: Slip bursts and creep events before the main instability

By looking at Figure 32 and tables 13,14 , the cumulated slip before the peak in friction ("peak slip", Fig. 32) and the main instability is controlled by four factors: a) the degree of alteration of rocks, b) slip cumulated by the creep events (or events with $V < 0.001$ mm/s), c) the magnitude of the slip bursts (or events with $V > 0.001$ mm/s), and d) the composition of the fluid involved.

The scatter of points in the bottom panel of figure 32 reflects the degree of alteration of the rocks even if less markedly than for the case of the effective normal stress (top panel): the more altered (= richer in L.O.I) Columbia River basalts have higher peak slip values than for CAMP basalts. The slip cumulated before the main instability (or peak slip) is given by the sum of slip bursts events plus slip cumulated during creep. In general, the average number of slip bursts is directly related to the slip cumulated (Fig. 33): H_2O+ CO_2 fluid experiments have on average more slip bursts, followed by H_2O and CO_2 fluid experiments. The large error bars for distilled H_2O and especially H_2O+CO_2 fluid experiments, are due to the large scatter of data for H_2O+CO_2

and H_2O fluid experiments (bottom panel of figure32); on the contrary, pure CO_2 fluid experiments have an higher degree of reproducibility. Therefore, peak slip depends, albeit to a lesser extent, on the composition of fluid in addition to the degree of alteration of the rocks.

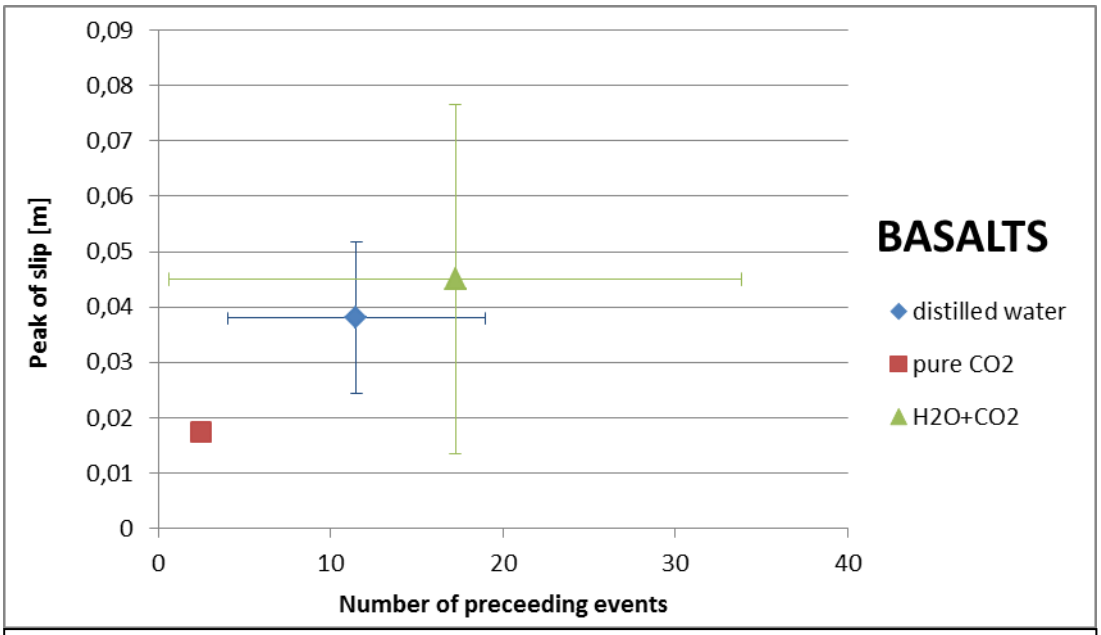

Figure 33: Peak of slip vs number of preceding events: mean values and std deviation

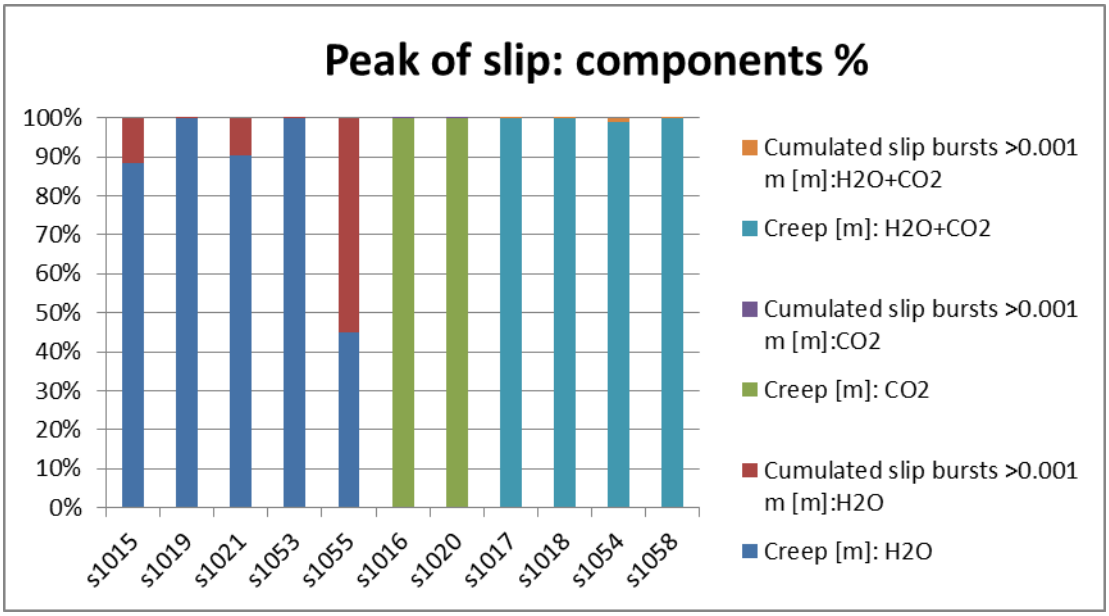

Fig.34: Histogram showing the different percentages of slip bursts and creep events during basalts experiments.

With few exceptions, even in those experiments characterized by an elevated number of slip bursts, ~90% of slip is cumulated by creep events, as seen in figure 34. The outlier is experiment s1055, in which 45% of peak slip was cumulated by creep and the residual part by slip bursts, despite the number of slip burst events is on the average.
The smaller slip cumulated by the creep event is caused by a vurst event of high slip velocity (~0.08 m/s): in fact we noticed that events with higher slip velocity run out later compared to the ones with lower velocity.

4.1.2:Chemical data

The concentration of the ion dissolved in the H_2O-rich fluids determined in the analysis after the experiments (Table 12) results from the (1) initial chemical composition of the water, (2) the chemical and mineralogical composition of the basalts, (3) the pH (P/T conditions), (4) the total slip cumulated in the tests and, (5) the grain size of the rock samples. Fluid samples collected after H_2O+CO_2 experiments had on average a higher Ca^{2+} and Mg^{2+} concentration with respect to experiments performed in (distilled) H_2O. In fact CO_2 is chemically activated by the presence of water, dissolving into the latter and producing carbonic acid H_2CO_3. This fluid interacts with basalt and leaches metal cations, such as Mg^{2+} , Ca^{2+} and Fe^{2+} (see reactions 3 to 6, introduction). Unfortunately we could not measure Fe^{2+} concentration because we could measure only the major elements, but we speculate that water was enriched also in this cation. In particular, we observed a linear increase in Ca^{2+} concentration with displacement: the greater is the displacement, the greater is the Ca content released from basalt into the mixture of H_2O+CO_2 (see table 12, experiments s1018, s1054, s1058). In fact, fault slip (with slip = V dt) produces frictional heat per unit of area Q:

$$dQ=\tau V\, dt \qquad \text{Eq.9}$$

Moreover, with progressive slip, original grains are reduced in gouge, which has higher specific surface, fostering metal release from basalts according to the pH of the mixture of H_2O+CO_2.

The pH at the peak of pressure (4 to 5.6 MPa) and the maximum temperature (15.8 to 24.9°C) recorded by the thermocouple during the main instability was extrapolated from fig.6c and it is approximately of 3.1-3.2. We do not believe that these pH variations may cause appreciable changes in mineral dissolution rates and ion production during the experiments. Besides this, possible limited variations in dissolution rate might be "covered" by the contamination of water due to residual tap water of previous tests in the pipes of the pressurising circuit. This contamination is proved by the presence of nitrate, sulphate and ammonium found in post–experimental fluids, as suggested by the composition of the collected tap water (table 12, Roma's tap water).

4.1.3: Evidence of mineral carbonation

In the case of the slipping zone produced in experiments performed on CAMP basalts immerged in pressurized H_2O+CO_2 fluids, we found calcite and dolomite grains with micro-Raman spectroscopy (Fig 28). If it is true that calcite may be found in basalts as secondary phase, for example as precipitation product in vacuoles (it does not apply to the rocks used in our experiments: we mainly found chalcedony as hole fillings), dolomite is an irrefutable proof of mineral carbonation. Calcite and dolomite formation under the deformation conditions reproduced in our experiments is described in reaction (2) (see introduction): fluids over-saturated in Ca and Mg react with CO_3^{2-} forming carbonates. This finding was a surprising result, in consideration of the short duration of our experiments (~30-40 min in total). These minerals formed in just few spots of the sliding surface, as witnessed by the low intensity of their Raman spectra (see Fig. 29). Therefore, we can state that calcite and dolomite formation did not affect the mechanical properties of the experimental faults, though their formation further supports the fact that our experiments reproduced conditions that might be achieved during storage of H_2O+CO_2 fluids (e.g., Carbfix) .

4.2:Carrara marble and interaction with H_2O- and CO_2- rich fluids

4.2.1:Mechanical data

Differently from basalts, in the case of Carrara marbles, the grain size, the chemical and mineralogical composition was about the same in all the experiments. Hence, the only parameter that varied was the composition of the fluid involved. In all the experiments, the peak effective friction μ_p' was about 0.5, independently of the fluid composition (pure H_2O, pure CO_2 and H_2O+CO_2 experiments). The frictional instability occurred at higher effective normal stress in the case of H_2O+CO_2 fluids, and lower effective normal stress for CO_2 and distilled H_2O. We did not observe the same negative linear trend as the one in figure 16 for the case of basalts, owing to variation in peak shear stress during the tests (in s1052 and s1057 $\tau_{peak} \simeq 4.5$ MPa, instead in s1056 $\tau_{peak} \simeq 4.8$ MPa). Weakening of Carrara marbles in the presence of H_2O+ CO_2 is explained by the dissolution reactions occurring at the rock surfaces: H^+ ions react with calcite , dissolving Ca^{2+} metals in solution:

$$CaCO_3 + H^+ = HCO_3^- + Ca^{2+}$$

The kinetics of calcite dissolution is favoured by the fine grain size of the comminuted (during shearing) Carrara marbles which results in a higher specific and reactive surface. Instead, the most surprising datum regards the experiment performed in CO_2 fluid. The main instability occurred at 9.5 MPa effective normal stress, intermediate between H_2O+CO_2 (9 MPa) and pure H_2O (9.75 MPa) (Fig. 17). I was expecting the CO_2 to behave like an inert, contributing only to increase the pore pressure inside the vessel, instead it weakened the marbles more than pure H_2O, which it was expected to produce both a chemical and a mechanical effect. Moreover, the presence of CO_2 fluid results in the highest number of precursory events and the highest value of cumulated slip before the main instability compared to the other experiments conducted with Carrara marble.

4.2.2 Chemical data:

Enrichment of Ca^{++} in fluids during H_2O + CO_2 experiments reflects the expected dissolution reactions of calcite: the presence of Mg^{2+} could be due to small amounts of dolomite present in the Carrara marble or of Mg in solid solution with Ca in the dissolved calcite (i.e., experiments performed in pure H_2O had a lower Mg and Ca content, probably resulting from thermal decomposition plus degassing CO_2 of calcite grains due to frictional heating during slip, as suggested by figure 31).

4.3:Comparison between basalt and calcite-built marbles

We reported in figure 35 our complete dataset: the values of the peak effective friction coefficient data at the main instability in basalt overlap with those of Carrara marbles for both effective normal stress and of slip. Moreover, the percentage of creep and slip bursts cumulated before the main instability is similar (>95% creep and ~5% cumulated slip bursts). The peak effective friction coefficient for Carrara marble immerged in pressurized CO_2 is achieved at a similar effective normal stress as in CAMP basalts in pure CO_2. This would suggest that pure CO_2 acts mainly as an inert. However, the mechanism leading to main instability in the two rocks could be different. As suggested by Violay et al. (2013; 2014), the main weakening processes in Carrara marbles under these deformation conditions could be subcritical crack growth by stress corrosion and hydrolytic weakening, whereas, in the case of basalts, flash heating and melting. The latter is attested by 1) the finding of adhesive wear microstructures, which suggest the achievement of high temperatures at the asperity scale during frictional sliding, especially after the main INSTABILITY EVENT .The presence of fluorine (F^-) in the case of basalt might indicate that the temperature reached was up to 260°C, the temperature corresponding to the Teflon decomposition with concomitant F^- leakage. Temperatures at the interface with Teflon are expected to be higher in the case of basalt because of melt extrusion (facilitating the termal diffusion towards the o-ring) and because the temperature increase in the case of Carrara Marble is buffered by the decarbonation reaction. Furthermore, the amount of dissolved Ca^{2+} in fluids recovered from experiments performed on basalts is comparable with Ca^{2+} concentration in fluids

from Carrara marble experiments (Table 12), suggesting that the higher temperature reached at the asperity scales in basalts might have triggered the kinetics of the breakdown reactions of feldspar and pyroxene (intro reaction 3-5).

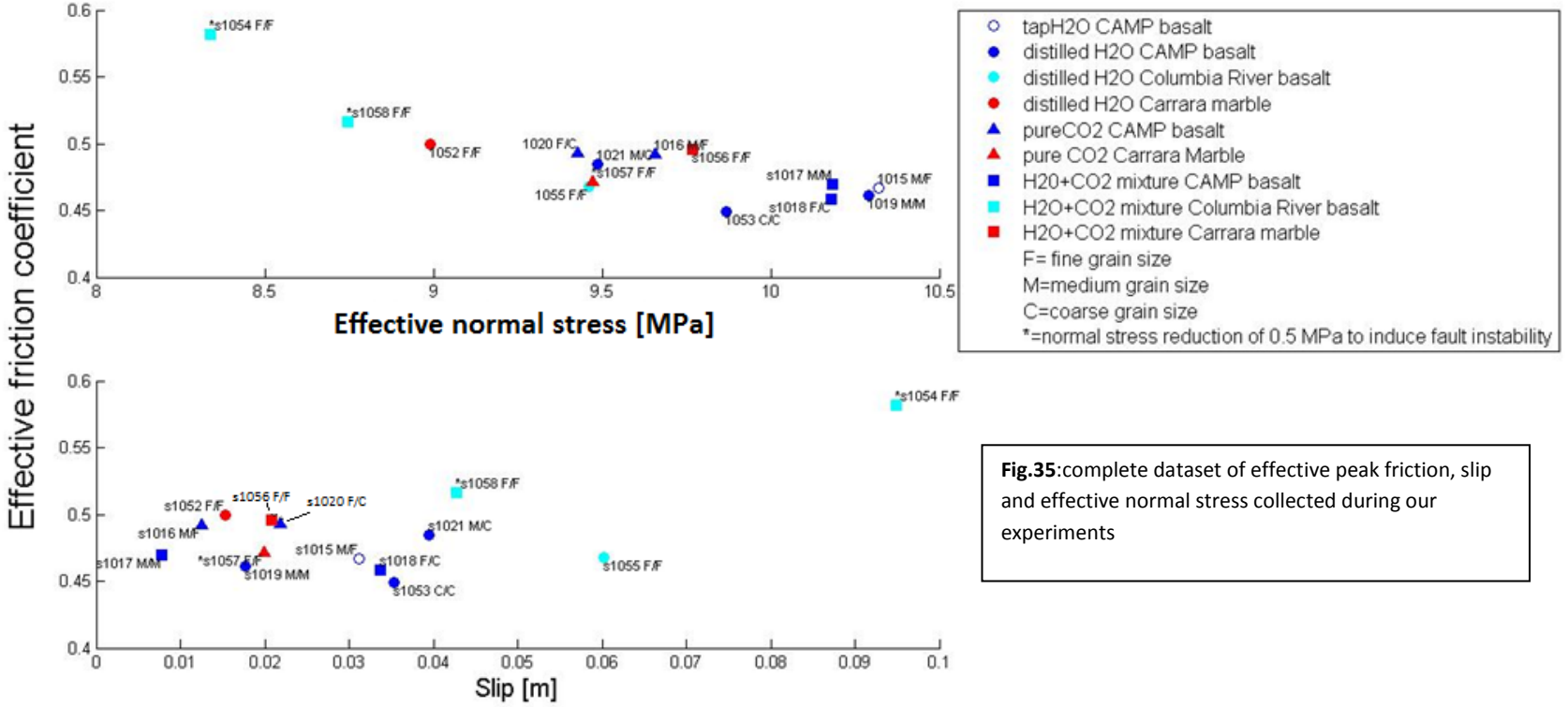

Fig.35:complete dataset of effective peak friction, slip and effective normal stress collected during our experiments

4.4:Implications for CO2 storage in basalts

Our experimental results suggest that injection of dry CO_2 (as in Wallula injection site, Mcgrail, 2006) results in a delayed (or at higher pore fluid pressures) reactivation of a critically stressed fault with respect the injection of H_2O+CO_2 mixtures (CarbFix project: Gislason, 2010) . On the other hand, the injection of H_2O+CO_2 mixture significantly speeds up mineral carbonation, reducing fluid leakage risks connected to pure CO_2 buoyancy. However this very rapid carbonation may create a dissolution/ precipitation wave, leading to the clogging of pores and thus creating a wall between the nearest portions of the injection well and the CO_2 reservoir.

Importantly, given the same composition of the fluid, the number of "foreshocks" of events preceding the main frictional instability decrease with the degree of alteration of the rocks. Conversely, a fault cutting altered rocks is more "silent" and reactivates without or with very few slip bursts.

4.5: Implications for seismicity in calcite-built rocks

Our few data collected on Carrara marble suggest that fault reactivates earlier in the presence of H_2O+CO_2 mixtures, due to Carrara marble-acidic water interaction. Hence, chemical activation of CO_2 by water plays an important role in fault-bearing carbonate re-activation. This is of fundamental importance in nature, because mantel CO_2 usually mixes with water during its ascent, causing weakening of carbonate rocks which is expected to be more marked than in the case of pure CO_2 and pure H_2O fluids. We remark the particular behaviour of Carrara marbles in the presence of pure CO_2 (fault reactivates at lower pore pressures than when pressurize by H_2O fluids). Given the limited dataset, it is suggested to perform further experiments in the future to obtain sound conclusions about the role of fluid composition in calcite-built rocks.

5.Conclusions

The large decrease in friction once the main instability is achieved suggests that pressurized experimental faults of basalts and calcite-built marbles are prone to be reactivated and generate earthquakes. This is well known in the literature, both for natural and man-induced earthquakes (Scholz, 2002 and reference therein). However, the experiments discussed in this thesis suggest the following:

1) the increase of fluid pressure in critically stressed faults leads to main frictional instabilities, independently of the composition of the fluid (pure CO_2, pure H_2O and CO_2+H_2O mixture);

2) more altered (i.e., with higher L.O.I. content) basalts (CAMP) are more prone to the main frictional instabilities than less altered basalts (Columbia River), independently of the composition of the fluids;

3) in basalts, given the same mineral composition and degree of alteration, injection of pure CO_2 delays fault reactivation (that is, higher fluid pressures are required to trigger the frictional instability);

4) in basalts, the total slip distance before the main instability is larger in less-altered basalts (Columbia River Basalts) than in more altered basalts (CAMP basalts);

5) in basalts, the number of slip bursts (or precursory events defined as slip events with 0.001 < slip rate < 0.3 m/s) before the main instability is lower in the presence of pure CO_2 than in pure H_2O and CO_2+H_2O mixtures;

6) in more altered basalts the frequency of precursory events decreased independently of fluid composition, making the experimental fault more “silent” than one made of less altered basalts;

7) in experiments performed in the presence of H_2O+CO_2 fluid mixtures, the concentration of Mg^{2+} and Ca^{2+} ion species was similar in both basalts and Carrara marbles and higher than in the case of pure H_2O experiments. In the case of the basalt experiments, the higher concentration of Mg^{2+} and Ca^{2+} was associated to carbonation reactions in the slipping zone (precipitation of calcite and dolomite); in the case of Carrara marble, the higher concentration of Mg^{2+} and Ca^{2+} was associated with lower

peak friction suggesting calcite dissolution as the main process responsible for fault weakening;

8) the rapid carbonation processes observed in the basalt experiments in the presence of CO_2+H_2O mixtures (they lasted only 30-40 minutes), demonstrates the great effectiveness of the large scale CO2 storage projects in basaltic rocks as the CarbFix in Iceland.

Concluding, in the case of CO_2 storage in basalts, pure CO_2 injection should result in delayed fault or fracture reactivation than in the case of CO_2+H_2O mixtures injection. However small variations in the content of altered minerals in basalts, would also control the occurrence of the main instability: more altered basalts could be more prone to frictional instabilities in the presence of pure CO_2 than less altered basalts in the presence of CO_2+H_2O mixtures.

Importantly, and differently to the injection of pure CO_2 fluids, the injection of CO_2+H_2O mixtures would result in fast deposition of carbonate minerals that will reduce the permeability of the reservoir. This, together with the very low concentration of CO_2 in H_2O (< 3%) would require continuous injection of fluids for hydrofracturing to increase the permeability of the reservoir permeability. Clearly, this will result in an increased seismic hazard in the area.

6.References

Bachu, Bonijoly, Brandshaw, Burruss, Halloway, Christensen, Mathiassen (2007). CO_2 storage capacity estimation: Methodology and Gaps. IJGGC I, 430-443.

Broz, M. E., R. F. Cook, and D. L. Whitney (2006), Microhardness, toughness and modulus of Mohs scale materials, Am. Mineral., 91, 135–142.

Byerlee, J. D. (1978), Friction of rocks, Pure Appl. Geophys., 116, 615–626.

Chiaraluce, L., Valoroso, L., Piccinini, D., Di Stefano, R., De Gori, P., 2011. The anatomy of the 2009 L'Aquila normal fault system (central Italy) imaged by high resolution foreshock and aftershock locations. J. Geophys. Res. 116, B12311, http://dx.doi.org/10.1029/2011JB008352.

Choi, Y. S., & Nešić, S. (2011). Determining the corrosive potential of CO 2 transport pipeline in high pCO 2–water environments. *International Journal of Greenhouse Gas Control*, *5*(4), 788-797.

Di Toro, G., Han, R., Hirose, T., De Paola, N., Nielsen, S., Mizoguchi, K., Ferri, F., Cocco, M., Shimamoto, T., 2011. Fault lubrication during earthquakes. Nature 471 (7339), 494–498, http://dx.doi.org/10.1038/nature09838.

Di Toro, G., Niemeijer, A., Tripoli, A., Nielsen, S., Di Felice, F., Scarlato, P.G., Spada, G., Alessandroni, R., Romeo, G., Di stefano, G., Smith, S., Spagnuolo, E., Mariano, S., 2010. From Geophys. field geology to earthquake simulation: a new state- of-the-art tool to investigate rock friction during the seismic cycle (SHIVA). Rend. Fis. Acc. Lincei 21, 95–114, http://dx.doi.org/10.1007/s12210- 010-0097-x.

Diamond, L. W., & Akinfiev, N. N. (2003). Solubility of CO 2 in water from− 1.5 to 100 C and from 0.1 to 100 MPa: evaluation of literature data and thermodynamic modelling. *Fluid phase equilibria*, *208*(1), 265-290.

El Hachimi H., Youbi N. Madeira J., Bensalah M.K., Martins L., Mata J., Medina F., Bertrand H., Marzoli A., Munha J., Bellieni G., Mahmoudi A., Abboui M., Assafari H. (2011). Morphology, internal architecture and emplacement mechanisms of lava flows from the Central Atlantic Magmatic Province (CAMP) of Argana Basin (Morocco). Geol. Soc. London Spec. Pub. 357, 167-193.

Gislason, Wolff-Boenisch, Stefansson, Oelkers, Gunnlangsson, Sigurdardottir, Sigfusson, Broecker, Matter, Stute, Axelsson, Fridriksson (2010). Mineral sequestration of carbon dioxide in basalt: A pre-injection overview of the CarbFix project. IJGGC 4, 537-545

Gudbrandsson, Wolff-Boenisch, Gislason , Oelkers (2008). Dissolution rates of crystalline basalt at pH 4 and 10 and 25-75°C. Mineralogical Magazine, Vol.72 (1), 155-158.

Hanley, E.J., Dewitt, D.P., Roy, R.F., 1978. The thermal diffusivity of eight well characterized rocks for the temperature range 300–1000 K. Eng. Geol. 12, 31–47.

Kelemen, Matter, Teagle (2014). Oman Drilling Proposal Project.

Kelemen, Matter (2008). In situ carbonation of peridotite for CO_2 storage. PNAS, US, 105,17,295-217,300.

Le Maitre, R.W., 2002. Igneous Rocks: A Classification and Glossary of Terms: Recommendations of the International Union of Geological Sciences Subcommission on the Systematics of Igneous Rocks. Cambridge University Press, UK. 240 p.

Miller,S.A.,Collettini,C.,Chiaraluce,L.,Cocco,M.,Barchi,M.,Kaus,B.J.P.,2004. Aftershocks drivenbyahigh-pressureCO2 source at depth. Nature427, 724–727.

Matter, Kelemen (2009). Permanent storage of carbon dioxide in geological reservoirs by mineral carbonation. Nature Geoscience, DOI:10.1038/NGEO683.

McGrail, Schaef, Ho , Chien, Dooley, Davidson (2006). Potential for carbon dioxide sequestration in flood basalt. Journal of Geophysical Research, vol.111, B12201.

Stefan Nielsen, Elena Spagnuolo, Marie Violay; Composite sample mount assembly (SAMOA): the ultimate sample preparation for rotary shear experiments. INGV Rapporti Tecnici. ISSN 2039-741, Anno 2012, Numero 215;

Oelkers, Gislason, Matter (2008). Mineral carbonation of CO_2. Elements, vol.4, 331-335.

Paterson, M. S., & Wong, T. F. (2005). *Experimental rock deformation-the brittle field*. Springer Science & Business Media.

J. Rutqvist , J. Birkholzer, F. Cappa, C.-F. Tsang. Estimating maximum sustainable injection pressure during geological sequestration of CO2 using coupled fluid flow and geomechanical fault-slip analysis. Energy Conversion and Management 48 (2007) 1798–1807.

Samuelson, Spiers (2012). Fault friction and slip stability not affected by CO_2 storage. Evidence from short term laboratory experiments on North Sea reservoir sandstones and caprocks. IJGGC 11S, S78-S90.

Scholz (2002). The mechanics of earthquakes and fulting. Cambridge Univ.Press, Cambridge.

Shimamoto, T., and A. Tsutsumi (1994), A new rotary-shear high-speed frictional testing machine: its basic design and scope of research (in Japanese with English abstract), *J. Tectonic Res. Group of Japan*, *39*, 65-78.

Stockmann, Wolff-Boenisch, Gislason, Oelkers (2011). Do carbonate precipitate after dissolution kinetics? 1: Basaltic glass. Chemical Geology 284, 306-316.

Terakawa, T., Zoporowski, A., Galvan, B., Miller, S.A., 2010. High-pressure fluid at hypocentral depths in the L'Aquila region inferred from earthquake focal mechanisms. Geology 38, 995–998, http://dx.doi.org/10.1130/G31457.1

van Noort, Spiers, Drury, Kandianis (2013). Peridotite dissolution and carbonation rates at fracture surfaces under condition relevant for in situ mineralization of CO_2,.Geochimica et Cosmochimica Acta 106,1-24.

Violay, M., Nielsen, S., Spagnuolo, E., Cinti, D., Di Toro, G., & Di Stefano, G. (2013). Pore fluid in experimental calcite-bearing faults: Abrupt weakening and geochemical signature of co-seismic processes. *Earth and Planetary Science Letters*, *361*, 74-84.

Violay, M., Nielsen, S., Gibert, B., Spagnuolo, E., Cavallo, A., Azais, P., ... & Di Toro, G. (2014). Effect of water on the frictional behavior of cohesive rocks during earthquakes. *Geology*, *42*(1), 27-30.

Waples, D.W., Waples, J.S., 2004. A review and evaluation of specific heat capacities of rocks, minerals, and subsurface fluids. Part 1: Minerals and nonporous rocks. Nat. Resour. Res. 13 (2), 13–130.

APPENDIX A: Determination of the dissolved inorganic carbon concentration

CO_2 dissolves in water according to the following equilibrium steps:

$$CO_{2(g)} \Leftrightarrow CO_{2(aq)} \quad (1)$$

Showing the equilibrium between the gaseous and dissolved CO_2.

$$CO_2(aq) + H_2O \overset{K_{hyd}}{\Leftrightarrow} H_2CO_3 \quad \text{(Hydration of aqueous } CO_2\text{)} \quad (2)$$

That is the equilibrium established between the dissolved CO_2 and the carbonic acid. The latter is a weak acid that dissociates in two steps, producing bicarbonate and carbonate ions

$$H_2CO_3 + H_2O \overset{K_{ca}}{\Leftrightarrow} H_3O^+ + HCO_3^- \quad \text{(Dissociation of carbonic acid)} \quad (3)$$

$$HCO_3^- + H_2O \overset{K_{bi}}{\Leftrightarrow} H_3O^+ + CO_3^{2-} \quad \text{(Dissociation of bicarbonate ion)} \quad (4)$$

At equilibrium the following equations can be used to evaluate the concentrations of the different carbonate forms

$$K_{hyd} = \frac{C_{H_2CO_3}}{C_{CO_2} C_{H_2O}} \quad (5)$$

$$K_{ca} = \frac{C_{H^+} C_{HCO_3^-}}{C_{H_2CO_3}} \quad (6)$$

$$K_{bi} = \frac{C_{H^+} C_{CO_3^{2-}}}{C_{HCO_3^-}} \quad (7)$$

where $C_{H_2CO_3}$, $C_{HCO_3^-}$, $C_{CO_3^{2-}}$, C_{H^+} are the molar concentrations (mol/L) of carbonic acid, bicarbonate ion carbonate ion and hydronium ion, respectively.

The equilibrium constants, *k*, are function of the temperature, but we have used for all calculations the equilibrium constant *K* at T=25°C, because the amount of variation was negligible in the temperature investigated range (15-30°C) :

$$K_{hyd}\ (25°C) = 2.58 \cdot 10^{-3} \quad (8)$$

$$K_{ca}\ (25°C) = 4.27 \cdot 10^{-7} \quad (9)$$

$$K_{bi}\ (25°C) = 4.67 \cdot 10^{-11} \quad (10)$$

Since K_{bi} is 4 order of magnitude lower than K_{ca}, it is reasonable to neglect the equilibrium of dissociation of bicarbonate ion.

<u>pH determination:</u>

Since dissociation of carbonic acid is kinetically slow, at equilibrium, only a small fraction (ca. 0.2 - 1%) of the dissolved CO_2 is actually converted to H_2CO_3. Hence, the equilibrium is shifted toward the left and most of the CO_2 remains as solvated molecular CO_2.

Therefore, the species that must be considered for the pH evaluation are the $CO_{2\,(aq)}$, and the bicarbonate ions, in accordance with the equilibrium (11).

At equilibrium in a CO2-water system, produced adding CO_2 to distilled water, the concentration of $CO_{2(aq)}$ is equal to the solubility of CO_2 in water decreased by the dissociated fraction x, i.e. the concentration of the dissociation products (12):

$$CO_{2(aq)} + 2\ H_2O_{(l)} \Leftrightarrow H_3O^+ + HCO_3^- \quad (11)$$

Equilibrium conditions: $[CO_2]-x \qquad x \qquad x \quad (12)$

At this point we applied equation (6) and solved the equation of 2nd order to get concentration of H_3O^+ (13):

$$x = [H_3O^+] = \frac{-k_{ca} + \sqrt{k_{ca}{}^2 + 4 \cdot [CO_2] \cdot k_{ca}}}{2} \quad (13)$$

pH is the negative logarithm of H_3O^+ (14):

$$pH = -\log [H_3O^+] \quad (14)$$

THESIS CORRIGENDA

Chapter 2

- pp. 29, Eq.3 : "$\sigma_{eff} = \sigma_n(1-\alpha P_f)$" should be replaced with "$\sigma_{eff} = \sigma n - \alpha P_f$"
- pp.29, Eq.4 : "$\mu_{eff} = \tau / \sigma_n(1- \alpha P_f)$" should be replaced with "$\mu_{eff} = \tau / (\sigma_n - \alpha P_f)$"
- pp.29, Line 23: "$\tau = \mu_{eff}\, \sigma_n\, (1-\alpha P_f)$" should be replaced with "$\tau = \mu_{eff}\, (\sigma_n - \alpha P_f)$"

It should be noted that these corrections do not affect any other expression or result, as the proper formulas were included in the MatLab code used to collect the data.

Chapter 3

- pp. 48,50; Figure caption 16, 17: "In the top panel : peak shear stress against effective pressure. In the middle: effective friction coefficient vs effective pressure. At the bottom panel: effective friction coefficient against slip" should be "In the top panel : effective friction coefficient vs effective pressure. At the bottom panel: effective friction coefficient against slip".
- pp.70, Figure 30: + s1056 Carrara Marble: H2O+CO2 should be added to the legend.
- pp.75, Line 22: "CO_2 which was regulated manually" should be "CO_2 pressure which was regulated manually"
- pp.78, Eq.7: "$T_f(i) = T_{room} + \dfrac{\frac{1}{\rho \cdot Cp \cdot \sqrt{\kappa \pi}} \cdot \int_0^t \frac{1}{2} \cdot \frac{\tau(t') \cdot V(t')}{\sqrt{t-t'}} dt}{c_w \cdot \rho_w}$" should be

$$"T_f(i) = T_{room} + \frac{1}{c_w \cdot \rho_w \sqrt{\kappa \pi}} \cdot \int_0^t \frac{1}{2} \cdot \frac{\tau(t') \cdot V(t')}{\sqrt{t-t'}} dt"$$

It should be noted that these corrections do not affect any other expression or result, as the proper formulas were included in the MatLab codes used to collect the data.

Chapter 4

- pp.89, Line 22: “especially after the main.” should be “especially after the main instability event.”

Appendix A

- pp. 98, (6); (7); Line 15: “C_{H+} ” should be “$C_{H_3O^+}$ ”